CHEMISTRY OF MATERIALS
Cite This: *Chem. Mater.* 2019, 31, 4953−4970
Perspective
pubs.acs.org/cm

Nanoconfining Optoelectronic Materials for Enhanced Performance and Stability†

Xiaoqing Kong, Kai Zong, and Stephanie S. Lee*

Department of Chemical Engineering and Materials Science, Stevens Institute of Technology, Hoboken, New Jersey 07030, United States

The solution processing of optoelectronic active layers promises to usher in a new era of technologies, from rollable displays to smart textiles, but critical challenges remain in the processing of these materials. While solution-based deposition of these compounds, including organic small-molecules and polymers and metal−halide perovskites, is key to driving down manufacturing costs, the rapid, uncontrolled nature of solution processing invariably results in the formation of kinetically trapped films, with heterogeneities and defects spanning multiple length scales that degrade device performance. Given such finite time, usually on the order of seconds, for molecules to organize as solvent evaporates from the active layers, the use of nanoporous scaffolds to select for desired crystallization outcomes is a promising approach to addressing this critical issue. As the size of crystals decreases, their surface free energy plays an increasingly important role in dictating their morphology and structure. By confining crystallization within the sub-micrometer pores of scaffolds, such surface free energy effects can be exploited to select for specific polymorphs and crystal orientations. In this Perspective, we highlight the use of nanoporous scaffolds to stabilize high-performing polymorphs of metal-halide perovskites, as well as guide the orientation of organic semiconductor crystals both laterally and vertically for optimized in-plane and out-of-plane charge transport, respectively. Critically, examples of scalable solution-phase deposition methods using nanoporous scaffolds are highlighted as potential targets for commercialization.

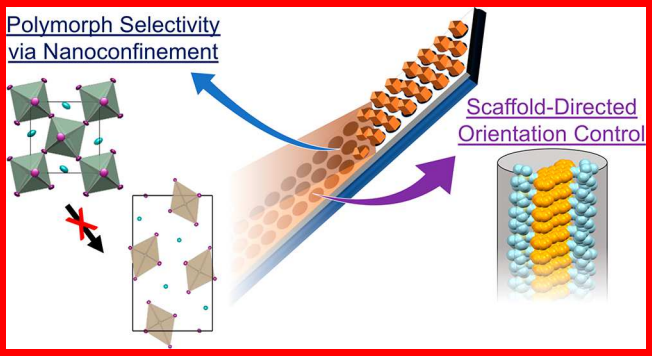

1. INTRODUCTION

Futuristic technologies, such as foldable newspapers with embedded videos and light-harvesting tinted windows, will be enabled through the use of flexible, inexpensive, and easily processed optoelectronic materials. These compounds, which can be solution-processed at room temperature and atmospheric pressure, will afford the high-throughput deposition of optically and electrically active layers over large areas and on flexible supports. Such soluble semiconducting compounds can generally be divided into three classes: polymers, small molecules, and metal−halide perovskites. While each type of material possesses unique advantages, tying them together is the ability to be dissolved in solution and subsequently rapidly deposited as thin films through different solution-based deposition methods, including inkjet printing, roll-to-roll coating, and spray coating.

One of the most critical challenges facing the widespread adoption of these materials in commercial applications is gaining control over the morphology of deposited films. A dichotomy exists in solution-processed semiconductor films—the ability to be rapidly processed from solution makes them highly desirable for the production of inexpensive electronics via large-scale manufacturing, but it is precisely this rapid processing that largely limits their device performance. In all three classes of materials, the extent of crystallinity and crystal size, orientation, and structure have a profound impact on the efficiency of optoelectronic processes, including charge transport, light absorption, and light emission. However, crystallization and morphological development are typically limited to the tens of seconds time scale as the solvent evaporates to leave behind a vitrified film. As a result, solution-processed films exist in kinetically trapped states with structural heterogeneities spanning multiple length scales.[1]

The impact of thin-film morphology on device performance is exemplified when comparing their performance to the gold standard of single crystals. Hole mobilities as high as 6.0 $cm^2/(V{\cdot}s)$, for example, have been measured for single crystals of a small-molecule organic semiconductor, fluorinated 5,11-bis-(triethylsilylethynyl) anthradithiophene (diF-TES ADT), grown by physical vapor transport. Spray-coated[2] and roll-coated[3] diF-TES ADT transistors, on the other hand, generally exhibit hole mobilities of around 1 $cm^2/(V{\cdot}s)$ or lower. Similarly, hole and electron diffusion lengths of greater than 175 μm have been measured in methylammonium lead iodide ($MAPbI_3$) single crystals,[4] but this number drops to 1 μm or lower in solution-processed active layers.[5] For organic solar

Received: April 30, 2019
Revised: June 18, 2019
Published: June 19, 2019

†This Perspective is part of the *Up-and-Coming* series.

DOI: 10.1021/acs.chemmater.9b01707
Chem. Mater. 2019, 31, 4953−4970

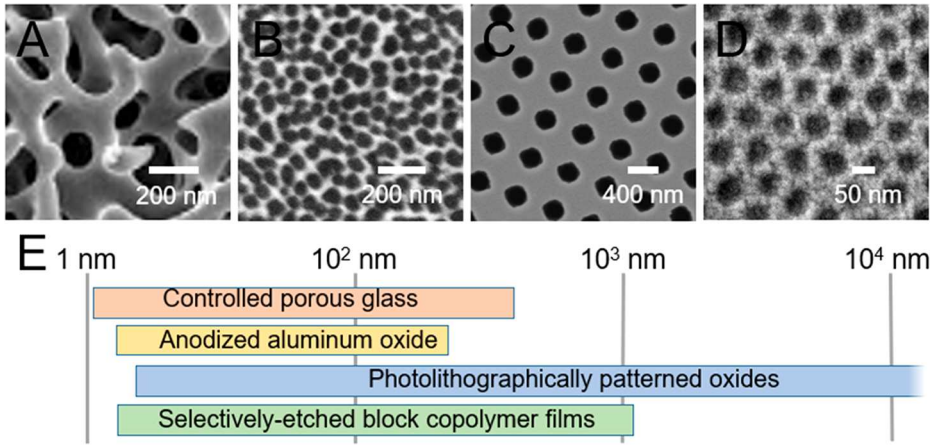

Figure 1. SEM images of nanoporous substrates used to confine crystallization, including (A) controlled porous glass (Adapted with permission from ref 26. Copyright 2009 Elsevier), (B) anodized aluminum oxide, (C) photolithographically patterned silicon substrates, and (D) selectively etched block copolymer films. (E) Approximate pore size ranges possible for each type of scaffold.

cells (OSCs) comprising polymer-based photoactive layers, the maximum theoretical efficiency is estimated to be between 20 and 24%,[6] while the highest reported OSC efficiency to date is 15.6%.[7] These top-performing devices are typically fabricated by batch spin coating. When fabricated using scalable industrial processes, OSCs have efficiencies of 6−7%.[8] In these systems, morphological control is expected to be the most significant challenge facing the improvement of solar conversion efficiencies toward the theoretical thermodynamic limit.[9]

The ideal morphology of solution-processed active layers depends on the final device application. For organic thin-film transistors, for example, charge is transported laterally through the active layer between the coplanar source and drain electrodes. In these devices, the optimum morphology comprises crystals oriented with the fast transport direction (i.e., the π-stack direction in organic small-molecule and polymer crystals) parallel to the substrate surface to align with the charge transport direction of the transistor. For OSCs and organic light-emitting diodes, on the other hand, charge transport occurs vertically through the active layer in a sandwich electrode configuration. In these devices, the fast charge transport direction should be aligned perpendicular to the substrate surface for maximum performance. In addition to crystal orientation, crystal structure also plays a critical role in determining device performance, with crystal polymorphism significantly affecting optoelectronic properties in all three classes of materials.[10,11,20,21,12−19]

Myriad strategies exist to control crystallization outcomes in solution-processed active layers, including post-annealing methods to relax structures into more thermodynamically favored states, solvent engineering, and the use of external forces, including shear flow and electric fields. The vast majority of these methods, however, have been developed for spun-cast films and are thus incompatible with continuous manufacturing methods. True morphological control will arise from the ability to dictate the location, orientation, and structure of nuclei during the earliest stages of film deposition before crystals form, and it is critical that such techniques be scalable for the future commercialization of such materials.

In this Perspective, we evaluate the use of nanoconfining scaffolds as a promising approach to dictate the morphology, including the crystal structure, orientation and size, of solution-processed active layers for optimized device performance in a variety of applications, including active matrix displays and light-harvesting photovoltaics. By confining crystal sizes to the tens to hundreds of nanometers length scale, we diverge from conventional principles governing bulk phase crystallization to achieve optimized structures and morphologies. At these dimensions, the surface free energy plays a critical role in determining crystallization outcomes. In section 2, we provide a brief overview of the rules governing nanoconfined crystallization compared to bulk crystallization, and highlight work done on systems across materials disciplines. Later sections focus on the use of nanoconfinement to guide crystallization outcomes in solution-processed optoelectronic materials, including polymorph control in metal−halide perovskites and orientation control in organic semiconductors. Finally, we provide an outlook on future directions in this field and highlight potential scalable methods to form nanoconfining scaffolds and thin films that will lead to the formation of high-performance optoelectronic active layers with optimized morphologies.

2. NANOCONFINED CRYSTALLIZATION

Nanoconfined crystallization of both organic and inorganic compounds has received sustained interest across materials disciplines, from pharmaceutics[22] to performance materials,[23] and is the topic of other comprehensive reviews.[24,25] After briefly reviewing available nanoconfining scaffolds and effects of nanoconfinement on crystallization outcomes in section 2, this Perspective will focus on the use of nanoconfinement to guide the crystallization of optoelectronic materials.

2.1. Nanoporous Substrates To Impose Confinement.

A variety of scaffolds have been used to confine the crystallization of molecular compounds on the nanometer to hundreds of nanometers length scale, including controlled porous glass (CPG), anodized aluminum oxide (AAO), photolithographically patterned substrates, and selectively etched block copolymer films. Examples of nanoporous scaffolds are provided in Figure 1. In general, these scaffolds nanoconfine solutions in two dimensions, with the third dimension unrestricted, as in the cylindrical nanopores of CPG (Figure 1A),[26] which has been used to study the nanoconfined crystallization of a number of compounds, including bisphenol M dicyanate ester,[27] pentaerythritol tetranitrate,[28] and acetaminophen.[22]

DOI: 10.1021/acs.chemmater.9b01707
Chem. Mater. 2019, 31, 4953−4970

Among these examples, AAO is the most widely used scaffold for nanoconfining crystallization. AAO scaffolds exhibiting ordered honeycomb arrays of cylindrical nanopores are formed via the electrochemical oxidation of aluminum films in acid solutions (Figure 1B).[29] Pore sizes can be varied from ~10 to 420 nm[30,31] by altering the anodization conditions, including the temperature, anodization time, voltage, and acid concentration,[32−35] as well as through a subsequent etching step. Unlike CPG, the cylindrical nanopores of AAO are uniaxially aligned, allowing for the use of X-ray diffraction to determine the orientation of crystals embedded within AAO relative to the long axes of the cylindrical nanopores. Over the past few decades, AAO has been widely used as a nanoconfining scaffold to control crystallization outcomes in materials including carbon nanotubes,[36] carbon nitride nanorods (CNRs),[37] liquid crystals,[38] polypyrrole,[39] poly(*N*-isopropylacrylamide),[40] calcium carbonate ($CaCO_3$),[41] DNA,[42] glycine derivatives,[43] glassy carbon,[44] among others.

Photolithography is also a common method to form ordered arrays of nanopores. These scaffolds are formed by spin coating a photoresist onto a target material, such as silicon oxide, and subsequently using a photomask or interference patterns to selectively expose the photoresist to light irradiation. Exposed areas can either be removed (i.e., negative photoresist) or retained (i.e., positive photoresist). The pattern formed by the photoresist can then be translated to the underlying substrate via an etching process that only takes place in the exposed regions. Compared to AAO, which forms ordered arrays through a self-assembly process, photolithographically defined scaffolds are more energy-intensive to fabricate. Photolithography has also been used to introduce nanoconfining lateral grooves to substrates.[45−48]

Based on compression molding methods in the polymer industry and pioneered by Chou and co-workers in 1996,[49] nanoimprint lithography is another type of lithographic technique that transfers patterns with nanoscale features from physical molds to polymeric substrates via imprinting. In a variation of this method termed "nanoparticle imprint lithography," Diao and co-workers used particles with spherical, square, and hexagonal geometries to create pores in polymer subsrtrates. Model aspirin crystals were found to preferentially orient in these pores depending on the registry between the angle made by the crystallographic planes of the faces of aspirin crystals and the angle presented at the pore corners.[50]

Compared to AAO and lithographically patterned porous substrates, microphase-separated block copolymer films are among the most promising scaffold materials for device incorporation due to their compatibility with large-scale manufacturing methods. These materials can be deposited from solution continuously via, for example, doctor blading and induced to self-assemble into periodic nanostructures with tunable dimensions depending on the relative lengths of the polymer blocks and the interaction parameter between them.[51] Different periodic nanostructures, such as lamellae, cylinders, gyroids, and spheres, with dimensions on the tens to hundreds of nanometer length scale can be obtained via microphase separation between the two chemically distinct blocks.[52−57] Upon microphase separation, nanocofinement effects of polymer chain alignment within individual phases have been observed in block copolymer systems comprising a crystallizing block.[58−60] To create nanoporous scaffolds, one block can be selectively etched, as displayed in Figure 1D.[61] The use of selectively etched block copolymer templates to direct crystallization has been studied for a variety of systems, including sol−gel derived silicon dioxide[62] and titanium dioxide,[63] ferroelectric poly(vinylidene fluoride-*co*-trifluoroethylene) (PVDF-TrFE),[64] niobium nitride superconductors,[65] and glycine.[66]

2.2. Polymorph Selectivity under Nanoconfinement.

Distinct crystal structures, or polymorphs, can exist in the same solid material and exhibit different solid-state properties, such as thermodynamic, kinetic, mechanical, surface, electronic, and optical properties.[67] Controlling polymorph outcomes represents a long-standing challenge to researchers across many fields, including pharmaceuticals,[68] organic electronics,[69,70] dyes,[71] explosives,[72] and food manufacturing.[73] Previous research has found that the kinetics and thermodynamics of crystallization at the nanoscale diverge from those in the bulk phase, leading to the formation and stabilization of metastable polymorphs in nanoconfined crystals.[22,24,25,66,74,75] While polymorph selectivity via nanoconfinement has been attributed to differences in the critical nucleus size of different polymorphs,[24] pore sizes as large as 250 nm, 2 orders of magnitude larger than the estimated critical nucleus size of molecular crystals, have also been found to influence the preferred polymorph compared to the bulk phase.[76]

The thermodynamically preferred polymorph corresponds to the phase with the lowest Gibbs free energy, G, at a given temperature and pressure. G in turn is a sum of the volume free energy, G_V, and the surface free energy, G_A. The change in G_V during solidification from the liquid phase upon undercooling, which results from the interatomic or intermolecular bonding energy, is always negative and stabilizing, whereas the change in G_A, which corresponds to the creation of an interface between the crystals and the surrounding medium, is always positive and destabilizing. The total surface free energy per mass unit can be written as $G_A = (\alpha/\rho)(A/V)$, where α is the average surface energy at the crystal surface, ρ is the corresponding bulk crystal density, A is the mean total surface area, and V is the mean volume per crystal. The total Gibbs free energy of crystals can thus be expressed as $G(T,A) = G_V(T) + (\alpha/\rho)(A/V)$.[77] For bulk systems with small surface-to-volume ratios, the contribution of G_A to the total Gibbs free energy is negligible. In nanocrystals characterized by high surface-to-volume ratios (A/V), however, the contribution of G_A to G becomes increasingly significant with decreasing particle size. In nanocrystals, G of a specific polymorph is thus not only a function of temperature, but also of crystal size. As the crystal decreases to a critical size, the contribution from the thermodynamically unfavorable surface free energy begins to outweigh the thermodynamically favorable volume free energy compared to other polymorphs, and consequently, the growth of nuclei into metastable polymorphs with a lower total Gibbs free energy is preferred.

Shifting of polymorph transition temperatures is thus a direct consequence of the increasing contribution of the surface free energy to the total Gibbs free energy with crystal size reduction. Figure 2 displays a general diagram of the Gibbs free energy of two polymorphs, α and β, in the bulk and nanoconfined phase. The α-phase is preferred at high temperatures, while the β-phase is preferred at lower temperatures. The point at which the Gibbs free energies are equal represents the solid-state transition temperature, $T_{\alpha\beta}$. Compared to the bulk phases, the nanoconfined phases both display higher Gibbs free energies due to an increased

DOI: 10.1021/acs.chemmater.9b01707
Chem. Mater. 2019, 31, 4953−4970

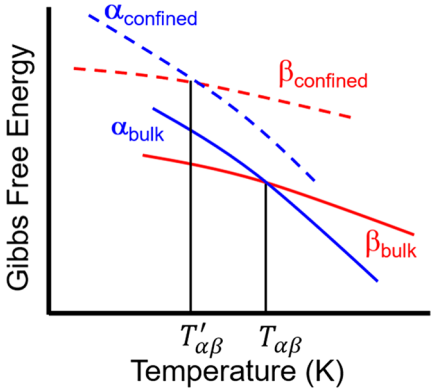

Figure 2. Gibbs free energy versus temperature diagram comparing different phases in the bulk and under nanoconfinement. Increasing the overall Gibbs free energies of both phases via nanoconfinement results in a lowering of the solid-state transition temperature.

contribution from the surface free energy. When the shift in the Gibbs free energy of the α-phase is smaller than that of the β-phase, as displayed in Figure 2, the phase transition temperature, $T'_{\alpha\beta}$, shifts lower compared to the bulk transition temperature. This scenario is expected for systems in which the surface free energy of the high-temperature α-phase is lower than that of the low-temperature β-phase and has been observed in a variety of nanocrystalline systems, including metal oxides and perovskites, such as Al_2O_3,[78] ZrO_2,[79] $MAPbI_3$,[80] and $PbTiO_3$.[81] For materials belonging to the perovskite and corundum families, as well as as ferroelectrics, ferromagnets, superconductors, and structural ceramics, it has been empirically observed that crystal lattices tend to transform into more symmetric structures as the crystal size decreases to the nanoscale.[82] This relationship, as mentioned above, is attributed to higher symmetry structures possessing smaller surface free energies compared to other polymorphs. Nanoconfinement can thus be an effective strategy to stabilize high-temperature polymorphs at near-ambient conditions.

2.3. Orientation Control via Nanoconfinement. In the bulk, crystal shapes are determined by the relative surface energies of different crystallographic planes, with crystals adopting morphologies that minimize their surface energy.[83,84] The exposed facets of a crystal thus represent the lowest surface energy crystallographic planes. From a kinetic standpoint, fast crystal growth occurs perpendicular to high-surface-energy planes to minimize the exposed surface areas of these faces. These growth rates are sensitive to the nature of the solvent[85] and the presence of molecular additives that preferentially attach to specific crystallographic faces.[86] Anisotropy in the structure of molecular compounds, such as those typical of organic semiconductors, can lead to significant differences in growth rates along different crystallographic directions. If the surface energy of one crystallographic plane is significantly higher than others, for example, needle-like crystals form.

Nanoconfinement presents a viable strategy to control the orientation of crystals through alignment of the fast growth direction with the long axis of the confining pores. Ward and co-workers proposed that crystal nuclei with their fast growth axis parallel to the pore direction can achieve the critical nucleus size needed to induce crystallization more rapidly than nuclei with their fast growth axis perpendicular to the pore direction.[24,87] As illustrated in Figure 3, nuclei must achieve a

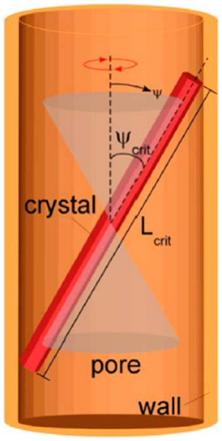

Figure 3. Illustration of orientation selectivity in nanoconfined pores in which nuclei can only achieve a critical nucleus length, L_{crit}, if the direction of the long axis is rotated at an angle $\psi < \psi_{crit}$. Adapted with permission from ref 24. Copyright 2012 American Chemical Society.

critical length, L_{crit}, to grow into crystals.[24] This critical length can only be achieved if the tilt angle, ψ, is smaller than the critical angle, ψ_{crit}. Nuclei oriented such that $\psi > \psi_{crit}$, on the other hand, will re-dissolve into the solution phase. Preferential orientation of molecular crystals in the uniaxially aligned cylindrical pores of AAO has been previously reported for poly(ethylene oxide) (PEO),[88] porous polystyrene-poly(dimethyl acrylamide) monoliths (p-PS-PDMA),[87] poly(vinylidene fluoride) (PVDF),[89,90] and tridecafluoro-1,1,2,2-tetrahydrooctyltrichlorosilane (FOTS),[91] among others, via 2D X-ray diffraction.

3. SHIFTING THE THERMODYNAMICS OF POLYMORPH TRANSITIONS IN METAL−HALIDE PEROVSKITES

Metal−halide perovskites (MHPs) have experienced a meteoric rise as being among the most promising active materials for solution-processed solar panels to date. Since their first application in solid-state solar cells in 2012,[92] the efficiencies of MHP solar cells comprising spun-cast active layers have recently surpassed over 22%.[93,94] Efficiencies of up to 19.6% have also been achieved using scalable solution-based deposition methods, such as roll-to-roll printing.[95] These materials typically adopt a 3D crystal structure with a stoichiometry of ABX_3. For organic−inorganic hybrid compounds, A represents an organic cation, such as methylammonium (MA) or formamidinium (FA), B represents a metal cation, such as Pb^{2+} or Sn^{2+}, and X represents a halide anion, such as I^- or Cl^-. All-inorganic compounds replace the organic cation with an inorganic one, such as Cs^+. The rich variety of compositional combinations affords precise tuning of the band gap of MHPs for efficient charge separation and transport to other layers. Beyond photovoltaics, other applications such as light-emitting diodes,[96] laser devices,[97] and photodetectors,[98] have also been investigated.

MHPs undergo temperature-dependent structural polymorph transitions that can significantly alter their optical and electronic properties.[99] These perovskites typically exist in at least three different polymorphs—a low-temperature orthorhombic phase, a tetragonal phase, and a high-temperature cubic phase, with the electrical conductivity positively correlated with the degree of symmetry of the crystal

DOI: 10.1021/acs.chemmater.9b01707
Chem. Mater. 2019, 31, 4953−4970

structure.[100] Generally, at temperatures between 300 and 400 K, methylammonium lead iodide ($MAPbI_3$) undergoes a reversible polymorph transition between the tetragonal polymorph (TP) and the higher symmetry cubic polymorph (CP) via the rotation of PbI_6 octahedra.[13] This phase transition temperature is within the operating temperature range of solar cells and may result in unwanted changes in the optoelectronic properties of the active layers during solar energy harvesting. A second low-temperature polymorph transition between orthorhombic polymorph (OP) and TP occurs in the range of 140 and 170 K.[101−103] Figure 4 displays

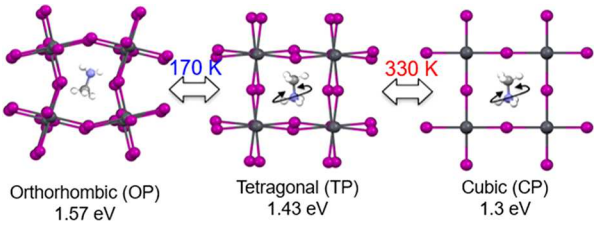

Figure 4. Solid-state transitions observed in bulk $MAPbI_3$ crystals.

the temperature-dependent polymorph transitions observed in bulk $MAPbI_3$. Such structural transitions in the perovskite film can affect the photovoltaic properties as the band gap increases with decreasing lattice symmetry.[104] The band gaps of the cubic, tetragonal and orthorhombic polymorphs of $MAPbI_3$, for example, have been calculated to be 1.3, 1.43, and 1.57 eV, respectively.[13] In one study, a sudden decrease of mobility was observed around the tetragonal−orthorhombic polymorph transition temperature due to this change in the band gap.[99] Accelerated recombination was also reported in the OP due to the small inclusions of TP, which act as charge recombination centers and are detrimental for photovoltaic performance.[101] As a result of these factors, a significant loss of PCE was observed near the tetragonal−orthorhombic transition.[105] In this section we will discuss the effect of nanoconfinement on both organic−inorganic MHPs (i.e., $MAPbI_3$) and all-inorganic MHPs (i.e., $CsPbI_3$).

3.1. Effect of Nanoconfinement on $MAPbI_3$ Polymorphism. Preventing polymorph transitions and stabilizing the high-temperature active phases of MHPs are critical to improving the performance of MHP-based solar cells. As mentioned in the previous section, crystals tend to adopt more symmetric structures as their sizes decrease to minimize the contribution from the surface free energy. Using chemical vapor deposition (CVD) to deposit $MAPbI_3$ into AAO templates with average pore sizes of 250 nm, Fan and co-workers discovered that the cubic phase of $MAPbI_3$ nanowires (NWs) is stabilized at room temperature (RT).[106] These NWs have desirable crystallinity and optical properties, and the embedded scaffolds can be incorporated into image sensors with extremely high resolution approaching the optical diffraction limit. Similar stabilization was reported for $MAPbI_3$ deposited into the interstices of close-packed polystyrene microspheres (PS-MSs) that decreased the perovskite crystal size to a range of 23−43 nm depending on the size of the PS-MSs.[107] Nanoconfinement was found to modify the intrinsic electronic states of perovskites, as manifested by absorption onset and PL peak shifts.

Using a solution-based method to deposit $MAPbI_3$ precursor solutions into AAO templates, we recently discovered that the cubic phase of $MAPbI_3$ was stabilized in the cylindrical pores of AAO templates to temperatures as low as 200 K, 133 K lower than the bulk transition temperature of 333 K.[80] As displayed in Figure 5A, $MAPbI_3$ crystals deposited on

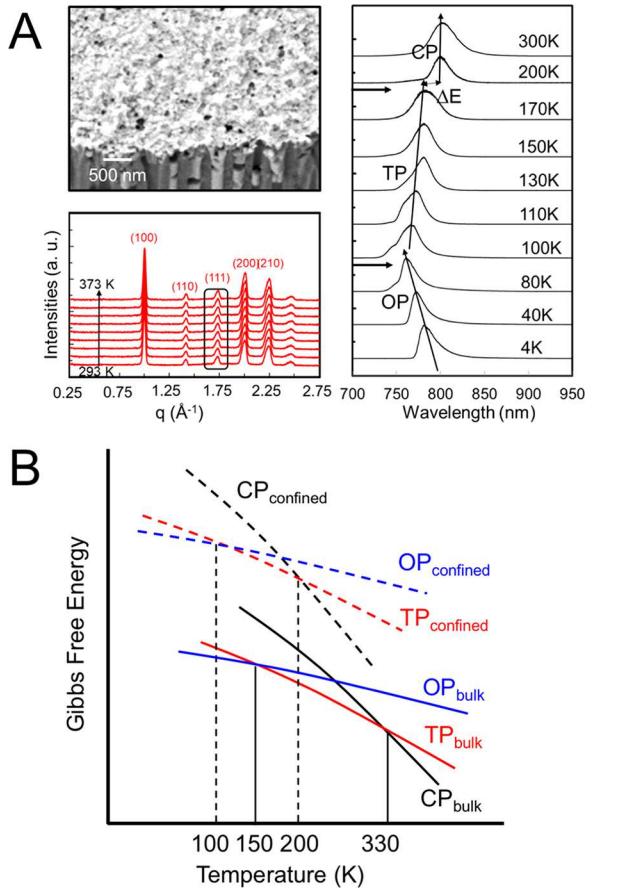

Figure 5. (A) SEM image of $MAPbI_3$ crystals embedded in a commercial AAO template with average pore sizes of 100 nm (top left). 1D line traces along q_{xy} = 0 $Å^{-1}$ extracted from in situ 2D XRD patterns collected on nanoconfined $MAPbI_3$ crystals at temperatures ranging from 293 to 373 K in increments of 10 K (bottom left). Peaks are indexed to the cubic phase of $MAPbI_3$. Normalized temperature-dependent PL spectra of nanoconfined $MAPbI_3$ measured at temperatures ranging from 4 to 300 K (right). Arrows denote shifts in the emission peaks, as well as the phase present. Horizontal black arrows near the y axis indicate solid-state phase transitions. Adapted with permission from ref 80. Copyright 2018 Royal Society of Chemistry. (B) Comparison of the proposed relative Gibbs free energies versus temperature of the different polymorphs in bulk and nanoconfined $MAPbI_3$ crystals, with phase transition temperatures labeled.

nanoporous AAO templates with an average pore size of 100 nm exhibited crystal sizes commensurate with that of the pore diameters. XRD patterns collected on these samples revealed that the confined crystals adopted the cubic phase at room temperature, identified by the presence of a single (111) peak at q = 1.75 $Å^{-1}$. In situ temperature-dependent XRD measurements further revealed that the reversible tetragonal-cubic phase transition of $MAPbI_3$, which occurs between 323 and 333 K in bulk crystals and is characterized by the splitting of the (111) peak of the cubic phase into separate peaks associated with the tetragonal phase, was absent in the range of 293−373 K in nanoconfined crystals.

DOI: 10.1021/acs.chemmater.9b01707
Chem. Mater. 2019, 31, 4953−4970

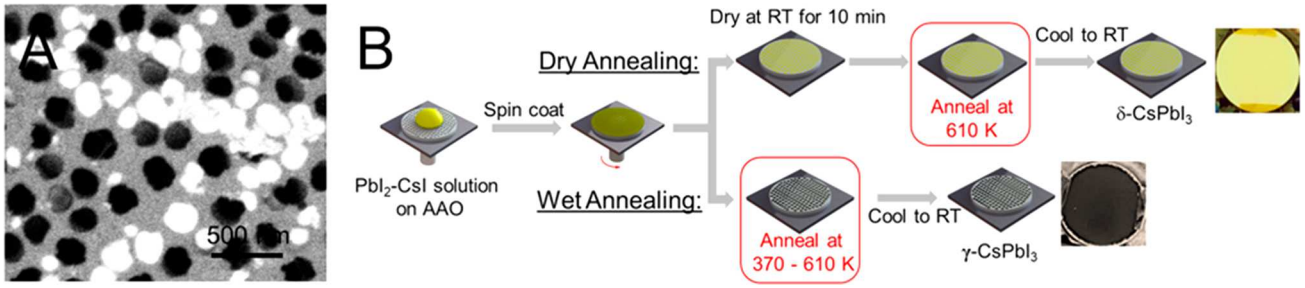

Figure 6. (A) Top-view SEM images of a representative AAO template infiltrated with a PbI_2/CsI mixture in DMF after wet annealing. (B) Infiltration of $CsPbI_3$ crystals in the nanopores of AAO templates via a dry annealing method, in which the solvent was allowed to completely evaporate prior to thermal annealing, and a wet annealing method, in which thermal annealing was performed on wet films immediately after solution deposition via spin coating. Adapted with permission from ref 76. Copyright 2019 American Chemical Society.

Taking advantage of the unique band gaps of each of the polymorphs, we further performed temperature-dependent confocal micro-PL spectroscopy (μPL) measurements across a temperature range of 4−300 K. Figure 5A displays the PL spectra as a function of temperature upon heating an AAO scaffold inifiltrated with $MAPbI_3$ crystals. As displayed in the figure, a single peak is observed for all temperatures measured. Abrupt shifts in the peak locations at 100 and 200 K were attributed to transitions from OP to TP and from TP to CP, respectively. The high-temperature CP remained stable even at 200 K, and the second polymorph transition of $MAPbI_3$ from TP to OP was suppressed to 100 K for $MAPbI_3$ crystals nanoconfined in AAO, 50 K lower than that of $MAPbI_3$ bulk crystals.

These observations on the shifted polymorph transition temperatures are consistent with an increase in the relative Gibbs free energies of the nanoconfined crystals compared to bulk crystals, as displayed in Figure 5B. In the bulk, OP has the lowest Gibbs free energy at low temperatures, TP at intermediate temperatures, and CP at higher temperatures. Upon nanoconfinement, the Gibbs free energy of each of the phases increases due to an increased contribution of the surface free energy. For nanoconfined crystals, the relative stabilities of the phases at different temperatures remain the same, but the solid-state transition temperatures are shifted to lower temperatures, in line with our experimental findings.

3.2. Effect of Nanoconfinement on $CsPbI_3$ Polymorphism. Compared with their organic−inorganic counterparts, all-inorganic perovskites, such as cesium lead iodide ($CsPbI_3$) and cesium tin iodide ($CsSnI_3$), have recently been explored as the active layer of electronic devices because of their excellent stability against moisture- and temperature-induced decomposition as well as competitive optoelectronic properties.[108,109] However, because the cesium cation is too small to form a stable perovskite crystal structure under ambient conditions, the high-performance active phases of $CsPbI_3$, namely, the α-, β-, and γ-phases, are typically only stable at elevated temperatures.[110] At room temperature, these perovskites adopt an inactive, non-perovskite δ-phase with wide band gaps of 2.8 and 2.6 eV, respectively.[111,112] Uncontrolled phase transitions to the inactive δ-phase not only preclude the use of these metastable perovskite phases in practical applications but also prevent the study of the intrinsic photophysical properties of the active $CsPbI_3$ polymorph at RT. It is thus of critical importance to stabilize active polymorphs with higher symmetry of perovskites at room temperature to improve the performance of electronic devices.

Scaling down the dimensions of $CsPbI_3$ crystals is being actively explored to stabilize the active phase at room temperature, as in the case of $CsPbI_3$ quantum dots with diameters on the nanometer length scale.[113−116] While many reports identify the room-temperature active phase as cubic α-$CsPbI_3$, recent studies suggest that in fact the structure is orthorhombic γ-$CsPbI_3$.[110,117,118] In the bulk, α-$CsPbI_3$ is stable at temperatures above 583 K,[100] while γ-$CsPbI_3$ is stable at temperatures between 448 and 533 K.[110] In agreement with these findings, recent density functional theory (DFT) calculations coupled with experiments found that γ-$CsPbI_3$ becomes thermodynamically preferred over δ-$CsPbI_3$ at room temperature at surface areas greater than 8600 m^2/mol.[119] This surface area corresponds to a spherical particle diameter of 69 nm.

Beyond the formation of nanometer-sized quantum dots, nanoconfining AAO scaffolds have been employed to reduce $CsPbI_3$ crystal dimensions to stabilize the active phase at room temperature. Using vapor-phase deposition to infiltrate AAO templates with $CsPbI_3$ crystals, Fan and co-workers stabilized an active phase of $CsPbI_3$ up to crystal diameters on the order of 200−250 nm, which they reported to be the α-phase.[120] These embedded single crystalline $CsPbI_3$ nanowires were stable in the presence of organic polar solvents, such as isopropyl alcohol, for at least 30 days, and the nanowire-embedded scaffolds were successfully incorporated into photodetectors. More recently, successful stabilization of the active phase of solution-deposited $CsPbI_3$ crystals has been reported using nanoporous AAO templates to restrict crystal dimensions. By systematically changing the pore size from 30 to 112 nm, Ma and co-workers identified a transition from the active phase of $CsPbI_3$, reported as the α-phase, to the inactive δ-phase above a pore size of 41 nm.[121] It was hypothesized that the active phase of $CsPbI_3$ is favored at the initial stages of crystallization due to an initial large surface area-to-volume ratio of the growing crystals. As the crystals grow, they either transform to the inactive δ-phase when the surface area-to-volume ratio falls below a critical value or are trapped in the active phase by the confining walls of the AAO scaffold. AAO scaffolds infiltrated with active $CsPbI_3$ were successfully incorporated into stable light-emitting diodes exhibiting electroluminescence at a wavelength of 702 nm with a narrow full width at half-maximum of 33 nm.

Using solution spin coating to infiltrate $CsPbI_3$ into AAO templates, we recently reported the stabilization of solution-deposited γ-$CsPbI_3$ in a temperature range of 4−610 K for characteristic crystal sizes of 250 nm,[76] six times larger than the transition size of 41 nm reported in the aforementioned study

DOI: 10.1021/acs.chemmater.9b01707
Chem. Mater. 2019, 31, 4953−4970

(Figure 6A). We attribute this expanded stability range to larger crystal sizes to the use of a wet annealing method that kinetically traps crystals in either the δ- or γ-phase, depending on the annealing temperature. As displayed in Figure 6B, precursor solutions were spun-cast onto AAO templates. If the solvent was allowed to dry completely before thermal annealing, i.e., the dry annealing method, $CsPbI_3$ became trapped in the inactive δ-phase, even when annealed at 610 K, 30 K above the bulk transition temperature of cubic α-$CsPbI_3$. On the other hand, if the infiltrated templates were annealed at 370 K or higher before the solvent completely evaporated, i.e., the wet annealing method, the γ-phase was adopted. Not only was the phase transition temperature found to shift from 448 to 370 K upon nanoconfinement but also temperature-dependent PL measurements revealed that the initial phase formed inside the nanopores became kinetically trapped, even to temperatures as low as 4 K. We expect that the nanopores prevent large volume expansion necessary to transition from the γ- to δ-phase. Nanoconfined γ-$CsPbI_3$ remained stable for at least 1 year of storage in air, the longest reported shelf life of this material to date.

3.3. Effect of Nanoconfinement on Perovskite Air Stability. In addition to shifting polymorph transition temperatures of metal−halide perovskites, it has been observed that nanoconfinement suppresses degradation mechanisms in these materials. Semitransparent solar cells incorporating AAO scaffolds to confine $MAPbI_{3-x}Cl_x$, for example, demonstrated suppressed ion migration.[122] In these devices, a cross-sectional view of which is displayed in Figure 7, the photocurrent

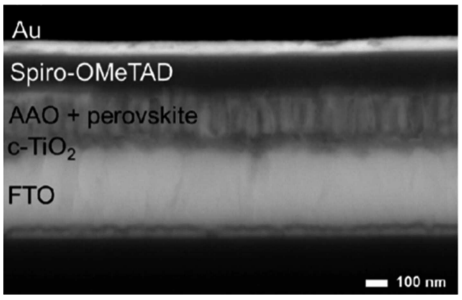

Figure 7. Cross-sectional SEM image of a perovskite solar cell incorporating an AAO scaffold to stabilize the perovskite layer against degradation. Adapted with permission from ref 122. Copyright 2016 Wiley.

decreased by only 30% after 2 h under continuous illumination of 1 sun and a constant temperature of 45 °C, while the planar perovskite solar cells fully degraded during this time under the same working conditions. This suppressed ion migration also reduced hysteresis in AAO-template nanopillar solar cells compared to their planar counterparts. Furthermore, the AAO-based solar cells showed higher PCE and V_{OC} values of 9.7% and 1.00 V, respectively, compared with planar solar cells with PCE and V_{OC} values of 8.1% and 0.77 V, respectively. It was also discovered that the decay process of photodetectors based on $MASnI_3$ embedded in AAO was slowed 840 times compared with that of a planar structure when exposed to air with 70% humidity.[123] In our system, 2D XRD patterns revealed that $MAPbI_3$ films deposited on flat SiO_2/Si substrates degraded into PbI_2 completely over a period of 21 days of exposure to air, while $MAPbI_3$ crystals nanoconfined in AAO templates exhibited no diffraction ring associated with PbI_2 after 594 days of storage in air with an average humidity of 60% without any chemical modification and passivation, the longest yet reported shelf life of $MAPbI_3$.[80] These significant improvements of perovskite stability can be attributed to the effective blockage of diffusion of water and oxygen molecules into the scaffolds. It is also reported that the nanoconfinement can increase the energy barrier of solid-state transitions requiring significant volume expansion or structural rearrangement, thus improving the stability of MHPs.[76]

Collectively, these reports suggest that nanoconfinement is a promising generalizable strategy to stabilize the active phase of MHPs by shifting the relative Gibbs free energies of the polymorphs, kinetically trapping desired polymorphs and preventing humidity-induced and other degradation mechanisms. Successful incorporation of nanoporous scaffolds into device architectures have already been demonstrated for field-effect transistors (FETs),[124] image sensors,[125] photodetectors,[120,123] and solar cell devices.[122] Looking forward, the use of selectively etched block copolymer scaffolds may present a promising strategy to nanoconfine crystals via scalable processing methods.

4. OPTIMIZING THE ORIENTATION OF ORGANIC SEMICONDUCTOR CRYSTALS

Unlike highly symmetric perovskite structures, organic semiconducting molecules and polymers are anisotropic in nature. In these systems, charge transport occurs via hopping through the π-orbital overlap network. Organic semiconductor crystals display large charge transport anisotropy along different crystallographic directions. In rubrene single crystals, for example, hole mobilities along the a and b axes were measured to be 4.4 and 15.4 $cm^2/(V{\cdot}s)$, respectively.[126] The 3-fold difference in mobility was attributed to stronger π-orbital overlap along the b axis compared to the a axis. Similar observations of charge transport anisotropy along different crystallographic directions have been reported for solution-processable compounds, including triisopropylsilylethynyl (TIPS) derivatives,[127,128] poly(3-hexylthiophene) (P3HT),[129−132] and poly(2,5-bis(3-alkylthiophen-2-yl)thieno-[3,2-b]thiophene) (PBTTT),[133,134] among others. Controlling both the in-plane and out-of-plane orientations of organic semiconductor crystals is thus critical to optimize device performance.

In organic semiconductors, the fast growth direction typically corresponds to the π-stack direction, with the π-plane representing a high-energy surface. Many small-molecule organic semiconductors, including trialkylsilylethynyl pentacenes,[135,136] N-trimethyltriindole,[137] and copper phthalocyanine,[138] form needle-like crystals in solution. In these crystals, the long axis of the needle corresponds to the π-stack direction, with the π-planes only exposed at the crystal tips. Because charge transport is fastest along the π-stack direction, orientation control is of particular importance to devices based on molecular and polymeric semiconductors and will depend on the device architecture. Figure 8 displays diagrams of an organic thin-film transistor (OTFT) with coplanar electrodes and an organic solar cell (OSC) with sandwich electrodes. In the former device, charge transport occurs laterally through the active layer (indicated by a red arrow). For maximum performance, the π-stack direction should be aligned parallel to the substrate surface. In OSCs, charge is transported vertically through the active layer, requiring the π-stack direction to be perpendicular to the substrate surface for

DOI: 10.1021/acs.chemmater.9b01707
Chem. Mater. 2019, 31, 4953−4970

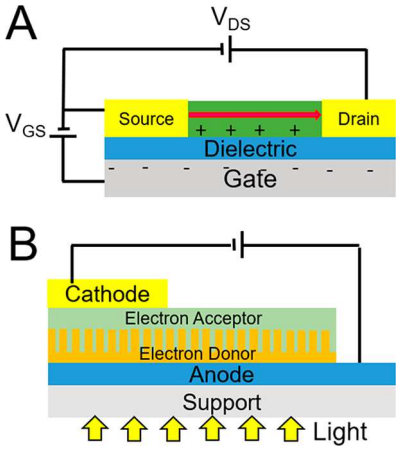

Figure 8. Diagrams of (A) a typical OTFT with coplanar electrodes and (B) an OSC with sandwich electrodes. Red arrow indicates the electron transport direction through the OTFT. The ideal interdigitated morphology between the electron donor and accept in the active layer of OSCs is displayed.

optimum performance. Ideally, the electron and hole transport layers would form an interdigitated structure with large surface area for exciton dissociation while maintaining continuous pathways through the donor and acceptor to the anode and cathode, respectively. The ability to control crystal orientation and size via nanoconfinement thus presents a unique opportunity to select optimized solution-processed active layers for specific applications.

4.1. Controlling In-Plane Crystal Orientation via Nanoconfinement. One of the most explored applications for solution-processed organic semiconductors is as active layers of OTFTs, basic components in displays and circuits. In these devices, charge transport occurs laterally through semiconductor films between coplanar source and drain electrodes (Figure 8A). To maximize performance, a large body of research has thus focused on controlling the in-plane orientation of semiconducting molecules in order to align the π-stack direction to the charge transport direction. Strategies have included solution shearing,[139−141] patterning the underlying substrate with different surface energies to guide crystallization,[142,143] temperature gradients,[129] and electric fields.[144−146] However, these methods typically result in polycrystalline films with grain boundaries that can impede charge transport.

Nanoconfinement of organic semiconductor solutions during crystallization is a promising scalable approach to form single crystalline organic semiconductor nanowires with orientations optimized for maximum charge transport. This method is based on the introduction of uniaxially aligned grooves to OTFT device platforms. These grooves, with widths ranging from the tens of nanometers to tens of micrometers, confine crystallization along a single direction chosen to be parallel to the charge transport direction. Preferential in-plane orientation of triisopropylsilylethynyl pentacene (TIPS-PEN) crystals, for example, was observed when crystallization was laterally confined within photolithographically patterned grooves with line widths ranging from 500 nm to 20 μm.[147] Panels A and B of Figure 9 display optical micrographs of TIPS-PEN crystals deposited on flat substrates and in 500 nm wide grooves, respectively, under cross-polarizers at two different angles. In the absence of confinement, TIPS-PEN

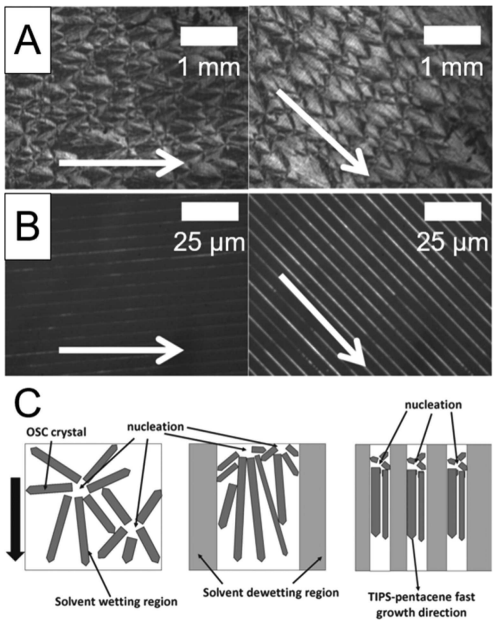

Figure 9. Optical micrographs of TIPS-PEN solutions deposited via solution shearing onto (A) flat substrates and (B) substrates with photolithographically patterned grooves. The micrographs were collected using cross-polarizers, with white arrows indicating the shear direction. (C) Illustration of the role of nanoconfinement in selecting for specific orientations of TIPS-PEN crystals. Adapted with permission from ref 147. Copyright 2014 Wiley.

crystals grew as elongated spherulites along the shear direction. Under cross-polarizers, bright and dark regions were visible at both angles of rotation (Figure 9A), indicating that multiple in-plane orientations were present. On the other hand, crystals deposited in the grooves displayed uniform birefringent behavior upon rotation of the sample between cross-polarizers, indicative of the formation of oriented, single TIPS-PEN crystals. The extent of orientation improved with decreasing width of the grooves due to increased selectivity for nuclei oriented with their fast growth axes aligned with the groove direction, as illustrated in Figure 9C. Hole mobilities of up to 2.7 $cm^2/(V{\cdot}s)$ were measured for OTFTs comprising TIPS-PEN crystals confined in 500 nm wide grooves, compared to 0.31 $cm^2/(V{\cdot}s)$ of those comprising unconfined TIPS-PEN crystals.

Based on a method originally developed to pattern polymer films,[148] variations of capillary force lithography have been developed to fabricate freestanding organic semiconductor wires on device platforms. This method relies on the use of a removable mold with microgrooves that confine organic semiconductor solutions during crystallization on a substrate surface. These molds can be subsequently removed to leave behind single crystal wires. In one of the earliest reports using this method, Jo and co-workers demonstrated the formation of highly oriented dioctylbenzothienobenzothiophene (C_8-BTBT) crystals within the microgrooves of a poly(dimethylsiloxane) (PDMS) stamp after contacting the stamp to a droplet of C_8-BTBT solution on a substrate.[149] Upon stamp removal, the crystals were found to be preferentially oriented with the π-stack direction parallel to the long axis of the grooves. OTFTs comprising oriented C_8-BTBT wires exhibited high average mobilities of 0.9 $cm^2/(V{\cdot}s)$.

DOI: 10.1021/acs.chemmater.9b01707
Chem. Mater. 2019, 31, 4953−4970

Using a similar method termed liquid-bridge-mediated nanotransfer molding (Lb-nTM), Park and co-workers demonstrated the generalizability of using polymeric molds to form freestanding, oriented organic semiconductor nanowire arrays.[150] Figure 10 displays the Lb-nTM fabrication

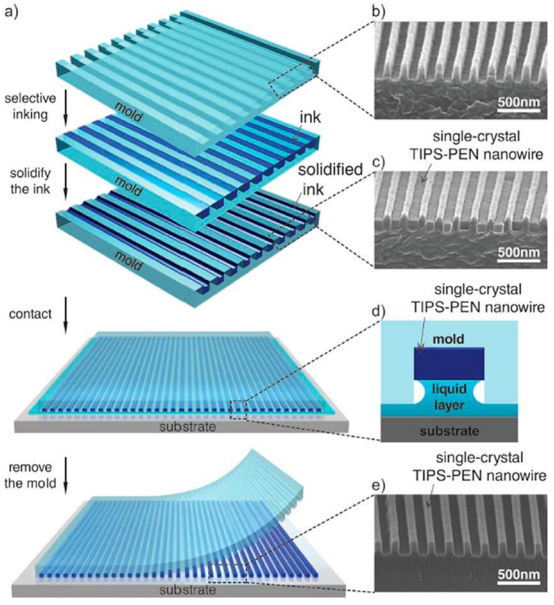

Figure 10. (A) Illustration of the LB-nTM method to crystallize organic semiconductors from solution in the nanogrooves of polymer molds. (B, C) SEM images of the mold before and after infiltration with TIPS-PEN, respectively. (D) Illustration of a TIPS-PEN nanowire inside a groove of the mold. (E) SEM image of a TIPS-PEN nanowire array upon removal of the polymer mold. Adapted with permission from ref 150. Copyright 2013 Wiley.

process, along with corresponding SEM images at each step. In this method, organic semiconductor solutions were infiltrated into PDMS molds via capillary forces and then transferred to substrate. Successful formation of TIPS-PEN, C_{60}, and P3HT nanowires with 90 nm diameters were demonstrated using this technique. Furthermore, selective-area electron diffraction patterns confirmed that all crystals adopted a preferential orientation. In the case of TIPS-PEN and P3HT, this orientation corresponded to the π-stack direction aligning with the long axis of the wires.

The use of submicrometer-wide grooves and channels to confine and direct the solution-phase crystallization of organic semiconductors has proven to be a widely generalizable strategy to control the orientation of solution-deposited organic semiconductor crystals. In addition to the examples highlighted above, nanoconfined crystallization in lateral grooves has also been applied to other small-molecule compounds, including a quinoidal oligothiophene derivative ($QQT(CN)_4$),[151] TIPS-PEN,[150,152,153] 8,16-didodecyl-8,16-dihydrobenzo[*a*]benzo[6,7]indolo[2,3-*h*]-carbazole (C12-BBICZ),[154] (triethylsilylethynyl)anthradithiophene (TES-ADT),[155,156] dioctylbenzothienobenzothiophene (C8-BTBT),[149] and 2,7-didecylbenzothienobenzothiophene (C10-BTBT),[157] and polymer semiconductors, including P3HT,[150,158−161] poly(9,9-dioctylfluorene-*alt*-bithiophene) (F8T2),[162] and diketopyrrolopyrrole-based polymers.[163]

4.2. Controlling Out-of-Plane Crystal Orientation via Nanoconfinement. For devices with sandwich electrode structures, such as solar cells, light-emitting diodes, and vertical transistors, the optimal orientation of organic semiconductor crystals is with the π-stack direction perpendicular to the substrate surface (Figure 8B). Such orientation has been achieved by thermally evaporating small-molecule organic semiconductors, including pentacene and zinc or copper phthalocyanine,[164−168] onto graphene surfaces. In these systems, strong interactions between the π-orbitals of the organic semiconductor molecules and underlying graphene surface cause the molecules to adopt a "lying-down" orientation. Solar cells comprising crystals with the π-stack direction perpendicular to the substrate surface were found to have 4-fold higher light conversion efficiences compared to solar cells with active layers comprising crystals in which the π-stack direction was parallel to the substrate surface.[165−168]

Controlling the out-of-plane orientation of solution-processable organic semiconductors, especially those comprising small molecules, has proven significantly more difficult. These molecules generally incorporate bulky solubilizing side groups that dominate molecule−substrate interactions. TIPS-PEN, for example, invariably adopts a "standing-up" molecular orientation with the π-stack direction parallel to the substrate surface. Few reports in the literature have demonstrated out-of-plane orientation control of solution-processed organic semiconductor thin films.[128,169] We recently discovered that TIPS-derivatized aromatic molecules with large acene cores can adopt two molecular orientations depending on the surface energy of the underlying substrate.[128] However, both orientations still resulted in the π-stack direction lying parallel to the substrate surface.

Nanoconfinement presents a promising strategy to control the out-of-plane orientation of organic semiconductors by aligning the long axes of the confining pores perpendicular to the substrate surface. Furthermore, restricting the diameter of crystals to lengths commensurate with exciton diffusion lengths in these materials, typically on the order of tens of nanometers, promotes efficient exciton dissociation. The use of AAO as templates to fabricate organic semiconductor nanostructures for OSC applications was the topic of recent reviews[170,171] and has been extensively examined for the templated growth of electrically active polymers via electrochemical deposition.[172−191] In this Perspective, we will highlight several examples in which nanoconfinement was used to control the out-of-plane orientation of organic semiconducting polymers and small molecules deposited via capillary forces into nanoconfining templates.

One of the most widely studied semiconducting polymers for OSC applications is regioregular P3HT. In thin films, P3HT chains typically orient with the long-chain axis parallel to the substrate surface. Fast interchain transport along the π-stack direction thus occurs in the plane of the film. In one of the first studies of P3HT infiltrated into AAO scaffolds with characteristic pore diameters ranging from 20 to 120 nm via capillary forces, Coakley and co-workers reported a 20-fold increase in hole mobility of P3HT nanowires compared to films.[192] This enhancement was attributed to preferential orientation of the P3HT chains within the nanowires. UV−visible spectroscopy measurements indicated that the extent of alignment increased with decreasing pore size. Following this work, Kim and co-workers used X-ray diffraction to confirm that nanoconfined P3HT chains adopt a "face-on" orientation with the π-stack direction parallel to the long axis of the confining pore.[193] An OSC incorporating P3HT nanopillars

DOI: 10.1021/acs.chemmater.9b01707
Chem. Mater. 2019, 31, 4953−4970

displayed a solar conversion efficiency of 1.12% compared to an efficiency of 0.17% for an OSC comprising a planar P3HT film.

Using pressure to infiltrate AAO scaffolds with solvent-swollen P3HT films at room temperature, Ding and co-workers examined the threshold for nanoconfinement-induced preferential orientation of P3HT chains to occur by varying the diameters of AAO scaffold pores from 60 to 130 nm.[194] As displayed in Figure 11, P3HT chains within the nanopillar

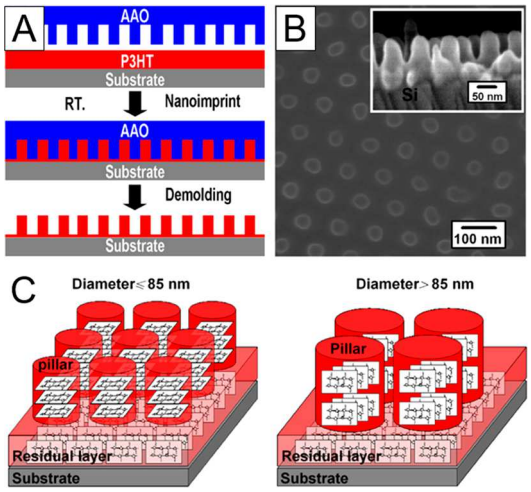

Figure 11. (A) Illustration of a nanoimprinting method to infiltrate AAO scaffolds with P3HT prior to scaffold removal to form freestanding P3HT nanopillars. (B) Top- and cross-sectional-view SEM images of P3HT nanopillars after scaffold removal. (C) Illustration of the preferred chain orientation within the nanopillars for pore sizes below (left) and above (right) 85 nm based on X-ray diffraction experiments. Adapted with permission from ref 194. Copyright 2013 American Chemical Society.

structures were found to adopt a face-on orientation when confined to space < 85 nm in diameter. Preferential orientation of P3HT chains under confinement was attributed to the alignment of the fast growth direction parallel to the long axis of the nanopores in the AAO scaffold. Similar preferred orientation of P3HT chains in the nanopores of AAO scaffolds has also been reported elsewhere,[195−197] while other reports found other orientations to be preferred, likely due to surface energy effects.[158,198,199] Beyond P3HT, preferential orientation of organic semiconductor crystals in AAO scaffolds with the π-stacking direction parallel to the long axes of the pores has also been reported for poly(3-dodecylthiophene)[200] and liquid crystalline 2-adamantonoyl-3,6,7,10,11-penta(1-butoxyl)-triphenylene[201] and hexabenzocoronene derivatives.[202,203]

Recently, Martín and co-workers demonstrated the preferential orientation of small-molecule organic semiconductor *p*-DTS(FBTTh$_2$)$_2$ deposited from the melt phase into the cylindrical nanopores of AAO.[204] As displayed in Figure 12, grazing incidence X-ray diffraction patterns revealed significant texturing of the diffraction pattern for *p*-DTS(FBTTh$_2$)$_2$ crystals confined in AAO scaffolds compared to that for bulk crystals. For pore sizes ranging from 40−400 nm, the crystals were found to orient with the (201) plane perpendicular to the long axes of the pores. This preferred orientation was attributed to the alignment of the fast growth axis with the pore direction. Interestingly, crystals confined within 25 nm pores were found to preferentially orient with the (141) plane

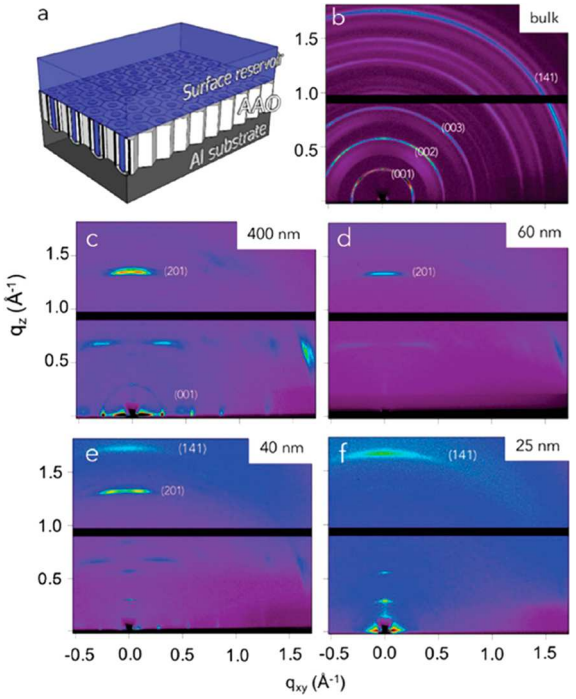

Figure 12. (A) Illustration of method to infiltrate p-DTS(FBTTh$_2$)$_2$ into AAO scaffolds. (B) 2D GIXD patterns of AAO scaffolds infiltrated with p-DTS(FBTTh$_2$)$_2$ crystals as a function of pore size. Adapted with permission from ref 204. Copyright 2018 Wiley.

perpendicular to the long axes of the pores. This plane corresponds to the π-plane of the molecule. It is unclear why this transition in preferred orientation occurred with decreasing pore size, but the authors note that both orientations have been observed along the long axes of *p*-DTS(FBTTh$_2$)$_2$ ribbons in thin films.[205]

5. DIRECTING UNCONFINED CRYSTAL GROWTH FROM SCAFFOLDS FOR HIGH-SURFACE AREA ARRAYS

One of the main drawbacks of using nanoporous scaffolds to guide crystallization outcomes is that the presence of the scaffold, which is typically insulating, interferes with optoelectronic processes. Scaffolds can be removed via harsh etching processes to leave behind nanowire arrays, or be lifted off after imprinting. In other cases, scaffolds have been incorporated directly into devices but limit the available surface area of the crystals that can participate in interfacial optoelectronic processes, such as exciton dissociation.

In an attempt to address this issue, we recently developed a novel method to use nanoconfinement to orient small-molecule organic semiconductor nuclei while allowing crystallization to proceed beyond the scaffold surface.[206] In this technique, 50 nm thick AAO scaffolds were fabricated directly onto device platforms, for example, TiO_2-coated ITO/glass. These substrates were then dip-coated in organic semiconductor solutions comprising triisopropylsilylethynyl-derivatized small molecules, such as TIPS-pyranthrene (TIPS-PY).[128,207] In the absence of an AAO scaffold layer, TIPS-PY crystals grew as needle-like crystals vertically from the substrate surface (Figure 13A). The average tilt of the crystals with respect to the substrate surface reflects the angle of 63° between the π-stack direction and the (010) plane of the TIPS

DOI: 10.1021/acs.chemmater.9b01707
Chem. Mater. 2019, 31, 4953−4970

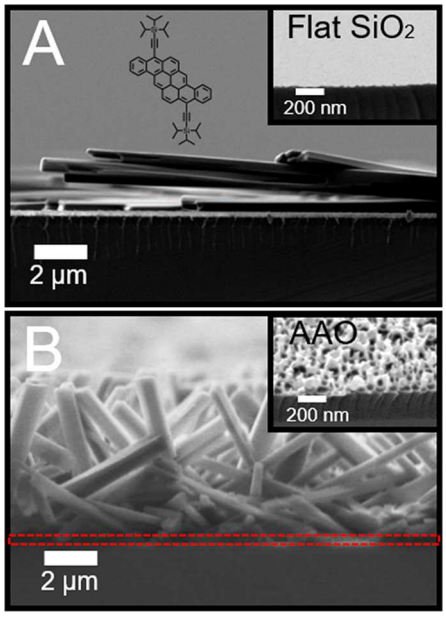

Figure 13. Side-view SEM images of a TIPS-PY film dip-coated onto a (A) SiO_2 substrate and (B) an AAO scaffold, respectively. The dashed red line in panel B indicates the AAO scaffold. Insets display side-view SEM images at a tilt angle of 35° of a flat SiO_2/Si substrate and a nanoporous AAO scaffold formed on SiO_2.

PY crystal structure, which lies parallel to the substrate surface. On the other hand, when dip-coated onto AAO scaffolds with average pore sizes ranging from 60 to 200 nm, TIPS-PY crystals grew with their long axes vertically from the substrate surface (Figure 13B). Single crystal X-ray diffraction experiments confirmed that the long axes of these needle-like crystals correspond to the π-stack direction. Photoluminescence intensity per unit surface coverage of the crystals was measured to be eight times higher for films comprising vertical crystals compared to those comprising horizontal crystals due to waveguiding along the crystal length.

To the best of our knowledge, these findings represent the first report of aligning the π-stack direction of crystals comprising organic semiconductor small molecules derivatized with solubilizing side groups perpendicular to the substrate surface. In this class of materials, crystal orientation has generally been observed to be dominated by side group−substrate interactions, invariably resulting in the π-stack direction lying parallel to the substrate surface. We speculate that the AAO scaffolds confine crystal nuclei formed at the air/solution/substrate interface during dip coating. Nuclei oriented with their fast growth direction parallel to the pore direction are selectively allowed to propagate vertically from the substrate surface. Because these crystals have a strong tendency to grow as needles, crystallization proceeds above the scaffold as solvent evaporates at the interface. In this manner, high-surface-area vertical crystal arrays can be formed without the need to remove the nanoporous scaffold.

Critically, this method is compatible with continuous coating methods, as displayed in Figure 14A, with crystal dimensions easily tuned by altering the processing parameters. By changing the dip coating rate and the characteristic pore size of the scaffolds, for example, we varied the crystal heights from 0.8 to 6.7 μm and crystal diameters from 0.1 to 0.6 μm of TIPS-PY vertical crystals. Panels B−D of Figure 14 display AAO scaffolds and corresponding TIPS-PY vertical crystal arrays formed on them via dip coating for characteristic scaffold pore sizes of 60, 100, and 200 nm. The average crystal diameters were found to correspondingly increase from 150 to 350 and to 650 nm, respectively. Overall, with morphologies and crystal orientations approaching the theoretical ideal for organic solar cells, such as vertical crystal arrays formed via continuous solution processing, address key challenges facing the solution-processed organic electronics community.

6. FUTURE OUTLOOK

Nanoconfining crystallization of organic and hybrid semiconductors presents a promising strategy to overcome the inherent limitations of rapid solution processing that afford little control over morphological development during film formation. Using nanoporous scaffolds, crystal dimensions, orientations, and polymorphs can be determined a priori and designed for optimal device performance. Already, tremendous progress has been made in the use of nanoconfining scaffolds to control crystallization outcomes of solution-processable small molecules, polymers, and metal−halide perovskites for optoelectronic applications, including photovoltaics, thin-film transistors, sensors, and photodetectors.

Looking forward, designing processes with scalability in mind will be necessary for future commercial success. In the light-harvesting field, for example, record efficiencies of OSCs

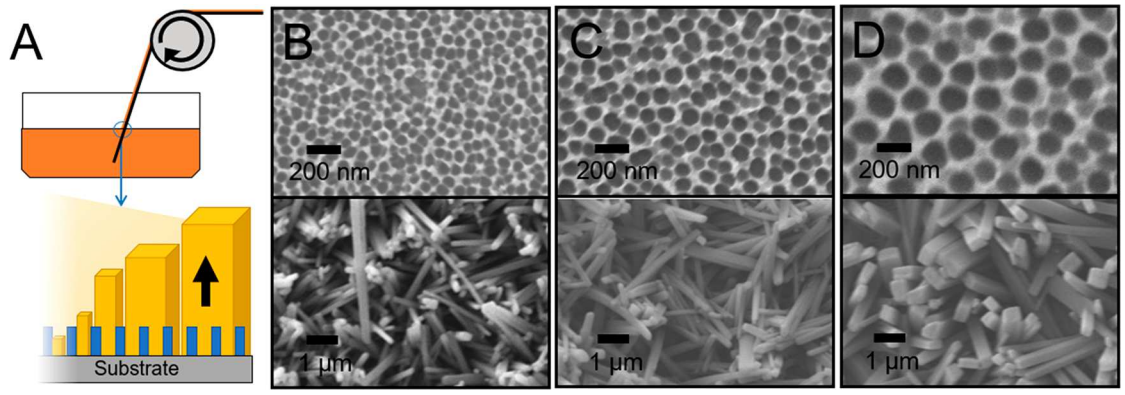

Figure 14. (A) Schematic of a continuous dip coating process to deposit vertical crystal arrays on nanostructured substrates, with a magnified illustration of directed nucleation at the air/solution/substrate interface. (B−D) SEM images of AAO scaffolds before and after vertical TIPS-PY crystal growth for characteristic pores sizes of 60, 100, and 200 nm.

DOI: 10.1021/acs.chemmater.9b01707
Chem. Mater. 2019, 31, 4953−4970

fabricated via continuous processing methods have consistently lagged behind those fabricated in the laboratory, with an average 40% decrease in solar conversion efficiency compared to the best performing devices with spun-cast active layers.[8] While nanoconfinement can improve the reproducibility and performance of these materials, strategies are needed to form nanoconfining scaffolds via continuous processing methods. Polymers that can either self-assemble into nanostructured arrays, such as those comprising block copolymers, or those that can be deposited as nanoporous scaffolds, for example through electrospinning, are strong candidates to address this challenge. We recently demonstrated successful use of an etched block colymer template to orient TIP-PY nuclei during dip coating. Figure 15 displays an SEM image of a polystyrene-

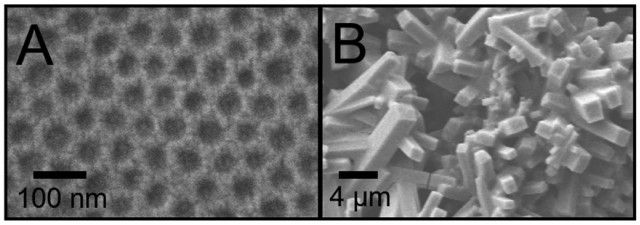

Figure 15. SEM micrographs of (A) a selectively etched block copolymer scaffold and (B) vertical TIPS-PY crystals deposited via dip coating onto the scaffold.

polylactide (PS-PLA) thin film in which the PLA was selectively etched using sodium hydroxide to leave behind cylindrical nanopores with average diameters of 40 nm. Promisingly, TIPS-PY also formed vertical crystals when deposited onto these scaffolds via dip coating.

Ultimately, fabricating nanoporous scaffolds out of materials that can actively participate in the optoelectronic processes will not only provide morphological control over the active layer but also contribute to the overall device performance and eliminate the need to remove the scaffold after active layer deposition. For solution-processed organic solar cells, an electron transport layer, such as titanium dioxide, is typically deposited on top of the cathode prior to active layer deposition. Compared to flat TiO_2 layers, TiO_2 layers with ordered nanoporous scaffolds via continuous processing methods would both exhibit a large interfacial area with the active layer for efficient charge transport and direct crystal growth in the solar cell active layer. These layers could also be fabricated from conductive polymers with tunable work functions. Such innovations will require contributions across materials disciplines, from chemical synthesis and interfacial chemistry to process engineering. Expanding the materials for nanoporus scaffolds that can be used for directing solution-phase crystallization not only will impact the solution-processed electronics community but will also have widespread implications for industries, including pharmaceutics, high-performance materials, and food manufacturing.

AUTHOR INFORMATION

Corresponding Author

*E-mail: stephanie.lee@stevens.edu.

ORCID

Stephanie S. Lee: 0000-0003-0964-6353

Notes

The authors declare no competing financial interest.

Biographies

Ms. Xiaoqing Kong is currently a Ph.D. candidate in the Chemical Engineering and Materials Science department at Stevens Institute of Technology. She obtained her M.S. degree in Materials Science from Stevens and Bachelor of Science degree in Polymer Science and Engineering from Sichuan University, China, in 2016 and 2013, respectively. Her research focuses on understanding the role of nanoconfinement in improving the performance and thermodynamic stability of metal halide perovskites. Through her research, she has reported unprecedented stability of nanoconfined $MAPbI_3$ and $CsPbI_3$ using nanoporous aluminum oxide scaffolds.

Mr. Kai Zong is currently a Ph.D. candidate in the Chemical Engineering and Materials Science department at Stevens Institute of Technology. He obtained his M.S. degree from Stevens and B.S. degree in Materials Science & Engineering from Taiyuan University of Technology in 2017 and 2010, respectively. At Stevens, he has pioneered the development of vertical crystal arrays using nanoporous aluminum oxide scaffolds and is the recipient of the Stevens Innovation and Entrepreneurship Doctoral Fellowship.

Prof. Stephanie Lee joined the Chemical Engineering and Materials Science department at Stevens Institute of Technology in 2014. She received her B.E. degree in Chemical Engineering from Massachusetts Institute of Technology and her M.A. and Ph.D. in Chemical Engineering and Materials Science from Princeton University in 2009 and 2012, respectively. She completed her doctoral work under the advisement of Prof. Yueh-Lin (Lynn) Loo as a National Defense Science and Engineering graduate fellow. From 2012 to 2014, she was a Postdoctoral and Transition Program for Academic Diversity Fellow in the Molecular Design Institute at New York University under the advisement of Prof. Michael D. Ward. At Stevens, her research focuses on the design of scalable processing methods, including twin-screw extrusion and scaffold-directed crystallization, of soluble organic and metal-hybrid semiconductors for optoelectronic applications. In 2019, she was the recipient of the NSF CAREER award for her proposed work on scaffold-directed organic semiconductor vertical crystal arrays.

ACKNOWLEDGMENTS

S.S.L. acknowledges financial support under NSF Awards ECCS-MRI-1531237 and CMMI-AM-1846178. K.Z. acknowledges support through the Stevens Innovation & Entrepreneurship Doctoral Fellowship. We are also grateful for support from the PSEG Foundation to advance energy innovation at Stevens. Microscopy resources within the Laboratory for Multiscale Imaging at Stevens Institute of Technology were used for this research.

REFERENCES

(1) Lee, S. S.; Loo, Y.-L. Structural Complexities in the Active Layers of Organic Electronics. *Annu. Rev. Chem. Biomol. Eng.* **2010**, *1*, 59−78.

(2) Azarova, N. A.; Owen, J. W.; McLellan, C. A.; Grimminger, M. A.; Chapman, E. K.; Anthony, J. E.; Jurchescu, O. D. Fabrication of Organic Thin-Film Transistors by Spray-Deposition for Low-Cost. *Org. Electron.* **2010**, *11*, 1960−1965.

(3) Temiño, I.; Del Pozo, F. G.; Ajayakumar, M. R.; Galindo, S.; Puigdollers, J.; Mas-Torrent, M. A Rapid, Low-Cost, and Scalable Technique for Printing State-of-the-Art Organic Field-Effect Transistors. *Adv. Mater. Technol.* **2016**, *1*, 1600090.

(4) Dong, Q.; Fang, Y.; Shao, Y.; Mulligan, P.; Qiu, J.; Cao, L.; Huang, J. Electron-Hole Diffusion Lengths > 175 mm in Solution-Grown $CH_3NH_3PbI_3$ Single Crystals. *Science* **2015**, *347*, 967−970.

DOI: 10.1021/acs.chemmater.9b01707
Chem. Mater. 2019, 31, 4953−4970

(5) Xiao, Z.; Dong, Q.; Bi, C.; Shao, Y.; Yuan, Y.; Huang, J. Solvent Annealing of Perovskite-Induced Crystal Growth for Photovoltaic-Device Efficiency Enhancement. *Adv. Mater.* **2014**, *26*, 6503−6509.
(6) Janssen, R. A. J.; Nelson, J. Factors Limiting Device Efficiency in Organic Photovoltaics. *Adv. Mater.* **2013**, *25*, 1847−1858.
(7) National Renewable Energy Laboratory. *NREL Efficiency Chart*; https://www.nrel.gov/pv/cell-efficiency.html.
(8) Carlé, J. E.; Helgesen, M.; Hagemann, O.; Hösel, M.; Heckler, I. M.; Bundgaard, E.; Gevorgyan, S. A.; Søndergaard, R. R.; Jørgensen, M.; García-Valverde, R.; Chaouki-Almagro, S.; Villarejo, J. A.; Krebs, F. C. Overcoming the Scaling Lag for Polymer Solar Cells. *Joule* **2017**, *1*, 274−289.
(9) Jackson, N. E.; Savoie, B. M.; Marks, T. J.; Chen, L. X.; Ratner, M. A. The Next Breakthrough for Organic Photovoltaics? *J. Phys. Chem. Lett.* **2015**, *6*, 77−84.
(10) Giri, G.; Verploegen, E.; Mannsfeld, S. C. B.; Atahan-Evrenk, S.; Kim, D. H.; Lee, S. Y.; Becerril, H. A.; Aspuru-Guzik, A.; Toney, M. F.; Bao, Z. Tuning Charge Transport in Solution-Sheared Organic Semiconductors Using Lattice Strain. *Nature* **2011**, *480*, 504−508.
(11) Fu, Y.; Rea, M. T.; Chen, J.; Morrow, D. J.; Hautzinger, M. P.; Zhao, Y.; Pan, D.; Manger, L. H.; Wright, J. C.; Goldsmith, R. H.; Jin, S. Selective Stabilization and Photophysical Properties of Metastable Perovskite Polymorphs of CsPbI3in Thin Films. *Chem. Mater.* **2017**, *29*, 8385−8394.
(12) Zhang, H.; Qiao, X.; Shen, Y.; Moehl, T.; Zakeeruddin, S. M.; Grätzel, M.; Wang, M. Photovoltaic Behaviour of Lead Methylammonium Triiodide Perovskite Solar Cells down to 80 K. *J. Mater. Chem. A* **2015**, *3*, 11762−11767.
(13) Baikie, T.; Fang, Y.; Kadro, J. M.; Schreyer, M.; Wei, F.; Mhaisalkar, S. G.; Graetzel, M.; White, T. J. Synthesis and Crystal Chemistry of the Hybrid Perovskite $(CH_3NH_3)PbI_3$ for Solid-State Sensitised Solar Cell Applications. *J. Mater. Chem. A* **2013**, *1*, 5628.
(14) Schulz, G. L.; Fischer, F. S. U.; Trefz, D.; Melnyk, A.; Hamidi-Sakr, A.; Brinkmann, M.; Andrienko, D.; Ludwigs, S. The PCPDTBT Family: Correlations between Chemical Structure, Polymorphism, and Device Performance. *Macromolecules* **2017**, *50*, 1402−1414.
(15) Fischer, F. S. U.; Kayunkid, N.; Trefz, D.; Ludwigs, S.; Brinkmann, M. Structural Models of Poly(Cyclopentadithiophene-*Alt*-Benzothiadiazole) with Branched Side Chains: Impact of a Single Fluorine Atom on the Crystal Structure and Polymorphism of a Conjugated Polymer. *Macromolecules* **2015**, *48*, 3974−3982.
(16) Galindo, S.; Tamayo, A.; Leonardi, F.; Mas-Torrent, M. Control of Polymorphism and Morphology in Solution Sheared Organic Field-Effect Transistors. *Adv. Funct. Mater.* **2017**, *27*, 1700526.
(17) Chung, H.; Diao, Y. Polymorphism as an Emerging Design Strategy for High Performance Organic Electronics. *J. Mater. Chem. C* **2016**, *4*, 3915−3933.
(18) Di Lorenzo, M. L.; Cocca, M.; Malinconico, M. Crystal Polymorphism of Poly(l-Lactic Acid) and Its Influence on Thermal Properties. *Thermochim. Acta* **2011**, *522*, 110−117.
(19) Corradini, P.; Guerra, G. Polymorphism in Polymers. In *Macromolecules: Synthesis, Order and Advanced Properties*, Vol. *100/1*; Springer-Verlag: Berlin, Heidelberg, 1992; pp 183−217, DOI: 10.1007/BFb0051637.
(20) Simone, S.; Curcio, E.; Di Profio, G.; Ferraroni, M.; Drioli, E. Polymeric Hydrophobic Membranes as a Tool to Control Polymorphism and Protein−Ligand Interactions. *J. Membr. Sci.* **2006**, *283*, 123−132.
(21) Stevens, L. A.; Goetz, K. P.; Fonari, A.; Shu, Y.; Williamson, R. M.; Brédas, J.-L.; Coropceanu, V.; Jurchescu, O. D.; Collis, G. E. Temperature-Mediated Polymorphism in Molecular Crystals: The Impact on Crystal Packing and Charge Transport. *Chem. Mater.* **2015**, *27*, 112−118.
(22) Beiner, M.; Rengarajan, G. T.; Pankaj, S.; Enke, D.; Steinhart, M. Manipulating the Crystalline State of Pharmaceuticals by Nanoconfinement. *Nano Lett.* **2007**, *7*, 1381−1385.
(23) Giesa, T.; Buehler, M. J. Nanoconfinement and the Strength of Biopolymers. *Annu. Rev. Biophys.* **2013**, *42*, 651−673.
(24) Hamilton, B. D.; Ha, J. M.; Hillmyer, M. A.; Ward, M. D. Manipulating Crystal Growth and Polymorphism by Confinement in Nanoscale Crystallization Chambers. *Acc. Chem. Res.* **2012**, *45*, 414−423.
(25) Jiang, Q.; Ward, M. D. Crystallization under Nanoscale Confinement. *Chem. Soc. Rev.* **2014**, *43*, 2066−2079.
(26) Beschieru, V.; Rathke, B.; Will, S. Particle Diffusion in Porous Media Investigated by Dynamic Light Scattering. *Microporous Mesoporous Mater.* **2009**, *125*, 63−69.
(27) Li, Q.; Simon, S. L. Surface Chemistry Effects on the Reactivity and Properties of Nanoconfined Bisphenol M Dicyanate Ester in Controlled Pore Glass. *Macromolecules* **2009**, *42*, 3573−3579.
(28) Xu, B.; Di, X.; McKenna, G. B. Melting of Pentaerythritol Tetranitrate (PETN) Nanoconfined in Controlled Pore Glasses (CPG). *J. Therm. Anal. Calorim.* **2013**, *113*, 539−543.
(29) Masuda, H.; Fukuda, K. Ordered Metal Nanohole Arrays Made by a Two-Step Replication of Honeycomb Structures of Anodic Alumina. *Science* **1995**, *268*, 1466−1468.
(30) Routkevitch, D.; Bigioni, T.; Moskovits, M.; Xu, J. M. Electrochemical Fabrication of CdS Nanowire Arrays in Porous Anodic Aluminum Oxide Templates. *J. Phys. Chem.* **1996**, *100*, 14037−14047.
(31) Li, A. P.; Müller, F.; Birner, A.; Nielsch, K.; Gösele, U. Hexagonal Pore Arrays with a 50−420 nm Interpore Distance Formed by Self-Organization in Anodic Alumina. *J. Appl. Phys.* **1998**, *84*, 6023−6026.
(32) Raoufi, M.; Tranchida, D.; Schönherr, H. Pushing the Size Limits in the Replication of Nanopores in Anodized Aluminum Oxide via the Layer-by-Layer Deposition of Polyelectrolytes. *Langmuir* **2012**, *28*, 10091−10096.
(33) Schwirn, K.; Lee, W.; Hillebrand, R.; Steinhart, M.; Nielsch, K.; Gösele, U. Self-Ordered Anodic Aluminum Oxide Formed by H_2SO_4 Hard Anodization. *ACS Nano* **2008**, *2*, 302−310.
(34) Michalska-Domańska, M.; Norek, M.; Stępniowski, W. J.; Budner, B. Fabrication of High Quality Anodic Aluminum Oxide (AAO) on Low Purity Aluminum—A Comparative Study with the AAO Produced on High Purity Aluminum. *Electrochim. Acta* **2013**, *105*, 424−432.
(35) Bai, A.; Hu, C.-C.; Yang, Y.-F.; Lin, C.-C. Pore Diameter Control of Anodic Aluminum Oxide with Ordered Array of Nanopores. *Electrochim. Acta* **2008**, *53*, 2258−2264.
(36) Lin, C.-C.; Chang, K.-C.; Pan, F.-M.; Kuo, C.-T.; Liu, M.; Mo, C.-N. Growth of Carbon Nanotube Field Emitters in the Triode Structure Using Anodic Aluminum Oxide as the Template. *Diamond Relat. Mater.* **2007**, *16*, 1388−1392.
(37) Yesuf, H. M.; Assen, M.; Melesse, A. M.; Alamirew, T. Detecting Land Use/Land Cover Changes in the Lake Hayq (Ethiopia) Drainage Basin, 1957−2007. *Lakes Reservoirs* **2015**, *20*, 1−18.
(38) Kim, H.; Ryu, S. H.; Tuchband, M.; Shin, T. J.; Korblova, E.; Walba, D. M.; Clark, N. A.; Yoon, D. K. Structural Transitions and Guest/Host Complexing of Liquid Crystal Helical Nanofilaments Induced by Nanoconfinement. *Sci. Adv.* **2017**, *3*, No. e1602102.
(39) Park, S. Self-Assembly of Mesoscopic Metal-Polymer Amphiphiles. *Science* **2004**, *303*, 348−351.
(40) Li, P.-F.; Xie, R.; Jiang, J.-C.; Meng, T.; Yang, M.; Ju, X.-J.; Yang, L.; Chu, L.-Y. Thermo-Responsive Gating Membranes with Controllable Length and Density of Poly(N-Isopropylacrylamide) Chains Grafted by ATRP Method. *J. Membr. Sci.* **2009**, *337*, 310−317.
(41) Lee, I.; Han, H.; Lee, S.-Y. Growth of Aragonite Calcium Carbonate Nanorods in the Biomimetic Anodic Aluminum Oxide Template. *J. Cryst. Growth* **2010**, *312*, 1741−1746.
(42) Kang, B.; Yeo, U.; Yoo, K.-H. Anodized Aluminum Oxide-Based Capacitance Sensors for the Direct Detection of DNA Hybridization. *Biosens. Bioelectron.* **2010**, *25*, 1592−1596.
(43) Amin, M. A. A Newly Synthesized Glycine Derivative to Control Uniform and Pitting Corrosion Processes of Al Induced by SCN− Anions − Chemical. *Corros. Sci.* **2010**, *52*, 3243−3257.

DOI: 10.1021/acs.chemmater.9b01707
Chem. Mater. 2019, 31, 4953−4970

(44) Rahman, S.; Yang, H. Nanopillar Arrays of Glassy Carbon by Anodic Aluminum Oxide Nanoporous Templates. *Nano Lett.* **2003**, *3*, 439−442.
(45) Motlagh, D.; Hartman, T. J.; Desai, T. A.; Russell, B. Microfabricated Grooves Recapitulate Neonatal Myocyte Connexin43 and N-Cadherin Expression and Localization. *J. Biomed. Mater. Res.* **2003**, *67A*, 148−157.
(46) Strittmatter, A.; Rodt, S.; Reißmann, L.; Bimberg, D.; Schröder, H.; Obermeier, E.; Riemann, T.; Christen, J.; Krost, A. Maskless Epitaxial Lateral Overgrowth of GaN Layers on Structured Si(111) Substrates. *Appl. Phys. Lett.* **2001**, *78*, 727−729.
(47) Natale, C. F.; Ventre, M.; Netti, P. A. Tuning the Material-Cytoskeleton Crosstalk via Nanoconfinement of Focal Adhesions. *Biomaterials* **2014**, *35*, 2743−2751.
(48) Park, S.; Lee, J.-M.; Ko, S. C. Fabrication Method for Passive Alignment in Polymer PLCs with U-Grooves. *IEEE Photonics Technol. Lett.* **2005**, *17*, 1444−1446.
(49) Chou, S. Y.; Krauss, P. R.; Renstrom, P. J. Imprint Lithography with 25-Nanometer Resolution. *Science* **1996**, *272*, 85−87.
(50) Diao, Y.; Harada, T.; Myerson, A. S.; Alan Hatton, T.; Trout, B. L. The Role of Nanopore Shape in Surface-Induced Crystallization. *Nat. Mater.* **2011**, *10*, 867−871.
(51) Bates, F. S.; Fredrickson, G. H. Block Copolymer Thermodynamics: Theory and Experiment. *Annu. Rev. Phys. Chem.* **1990**, *41*, 525−557.
(52) Park, M.; Harrison, C.; Chaikin, P. M.; Register, R. A.; Adamson, D. H. Block Copolymer Lithography: Periodic Arrays of ∼1011 Holes in 1 Square Centimeter. *Science* **1997**, *276*, 1401−1404.
(53) Cheng, J. Y.; Ross, C. A.; Smith, H. I.; Thomas, E. L. Templated Self-Assembly of Block Copolymers: Top-Down Helps Bottom-Up. *Adv. Mater.* **2006**, *18*, 2505−2521.
(54) Lazzari, M.; López-Quintela, M. A. Block Copolymers as a Tool for Nanomaterial Fabrication. *Adv. Mater.* **2003**, *15*, 1583−1594.
(55) Cheng, J. Y.; Ross, C. A.; Thomas, E. L.; Smith, H. I.; Vancso, G. J. Templated Self-Assembly of Block Copolymers: Effect of Substrate Topography. *Adv. Mater.* **2003**, *15*, 1599−1602.
(56) Yoon, E.; Kim, E.; Kim, D.; Son, J. G. Top-Coat Dewetting for the Highly Ordered Lateral Alignment of Block Copolymer Microdomains in Thin Films. *Adv. Funct. Mater.* **2015**, *25*, 913−919.
(57) Kim, E.; Kim, W.; Lee, K. H.; Ross, C. A.; Son, J. G. A Top Coat with Solvent Annealing Enables Perpendicular Orientation of Sub-10 nm Microdomains in Si-Containing Block Copolymer Thin Films. *Adv. Funct. Mater.* **2014**, *24*, 6981−6988.
(58) Sun, Y.-S.; Chung, T.-M.; Li, Y.-J.; Ho, R.-M.; Ko, B.-T.; Jeng, U-S.; Lotz, B. Crystalline Polymers in Nanoscale 1D Spatial Confinement. *Macromolecules* **2006**, *39*, 5782−5788.
(59) Huang, P.; Zhu, L.; Cheng, S. Z. D.; Ge, Q.; Quirk, R. P.; Thomas, E. L.; Lotz, B.; Hsiao, B. S.; Liu, L.; Yeh, F. Crystal Orientation Changes in Two-Dimensionally Confined Nanocylinders in a Poly(Ethylene Oxide)-b-Polystyrene/Polystyrene Blend. *Macromolecules* **2001**, *34*, 6649−6657.
(60) Loo, Y.-L.; Register, R. A.; Adamson, D. H. Polyethylene Crystal Orientation Induced by Block Copolymer Cylinders. *Macromolecules* **2000**, *33*, 8361−8366.
(61) Guarini, K. W.; Black, C. T.; Milkove, K. R.; Sandstrom, R. L. Nanoscale Patterning Using Self-Assembled Polymers for Semiconductor Applications. *J. Vac. Sci. Technol., B: Microelectron. Process. Phenom.* **2001**, *19*, 2784.
(62) Tseng, W.-H.; Chen, C.-K.; Chiang, Y.-W.; Ho, R.-M.; Akasaka, S.; Hasegawa, H. Helical Nanocomposites from Chiral Block Copolymer Templates. *J. Am. Chem. Soc.* **2009**, *131*, 1356−1357.
(63) Hsueh, H.-Y.; Ho, R.-M. Bicontinuous Ceramics with High Surface Area from Block Copolymer Templates. *Langmuir* **2012**, *28*, 8518−8529.
(64) Kang, S. J.; Bae, I.; Shin, Y. J.; Park, Y. J.; Huh, J.; Park, S. M.; Kim, H. C.; Park, C. Nonvolatile Polymer Memory with Nanoconfinement of Ferroelectric Crystals. *Nano Lett.* **2011**, *11*, 138−144.
(65) Robbins, S. W.; Beaucage, P. A.; Sai, H.; Tan, K. W.; Werner, J. G.; Sethna, J. P.; DiSalvo, F. J.; Gruner, S. M.; Van Dover, R. B.; Wiesner, U. Block Copolymer Self-Assembly−Directed Synthesis of Mesoporous Gyroidal Superconductors. *Sci. Adv.* **2016**, *2*, No. e1501119.
(66) Hamilton, B. D.; Hillmyer, M. A.; Ward, M. D. Glycine Polymorphism in Nanoscale Crystallization Chambers. *Cryst. Growth Des.* **2008**, *8*, 3368−3375.
(67) Diao, Y.; Lenn, K. M.; Lee, W. Y.; Blood-Forsythe, M. A.; Xu, J.; Mao, Y.; Kim, Y.; Reinspach, J. A.; Park, S.; Aspuru-Guzik, A.; Xue, G.; Clancy, P.; Bao, Z.; Mannsfeld, S. C. B. Understanding Polymorphism in Organic Semiconductor Thin Films through Nanoconfinement. *J. Am. Chem. Soc.* **2014**, *136*, 17046−17057.
(68) Beyazkilic, P.; Yildirim, A.; Bayindir, M. Nanoconfinement of Pyrene in Mesostructured Silica Nanoparticles for Trace Detection of TNT in the Aqueous Phase. *Nanoscale* **2014**, *6*, 15203−15209.
(69) Chen, J.; Anthony, J.; Martin, D. C. Thermally Induced Solid-State Phase Transition of Bis(Triisopropylsilylethynyl) Pentacene Crystals. *J. Phys. Chem. B* **2006**, *110*, 16397−16403.
(70) Poelking, C.; Andrienko, D. Effect of Polymorphism, Regioregularity and Paracrystallinity on Charge Transport in Poly(3-Hexylthiophene) [P3HT] Nanofibers. *Macromolecules* **2013**, *46*, 8941−8956.
(71) Yu, L.; Stephenson, G. A.; Mitchell, C. A.; Bunnell, C. A.; Snorek, S. V.; Bowyer, J. J.; Borchardt, T. B.; Stowell, J. G.; Byrn, S. R. Thermochemistry and Conformational Polymorphism of a Hexamorphic Crystal System. *J. Am. Chem. Soc.* **2000**, *122*, 585−591.
(72) Kim, W.; Gwak, M. C.; Lee, Y. H.; Yoh, J. J. A Two-Phase Model for Aluminized Explosives on the Ballistic and Brisance Performance. *J. Appl. Phys.* **2018**, *123*, No. 055902.
(73) Loisel, C.; Keller, G.; Lecq, G.; Bourgaux, C.; Ollivon, M. Phase Transitions and Polymorphism of Cocoa Butter. *J. Am. Oil Chem. Soc.* **1998**, *75*, 425−439.
(74) Ha, J. M.; Hamilton, B. D.; Hillmyer, M. A.; Ward, M. D. Phase Behavior and Polymorphism of Organic Crystals Confined within Nanoscale Chambers. *Cryst. Growth Des.* **2009**, *9*, 4766−4777.
(75) Graubner, G.; Rengarajan, G. T.; Anders, N.; Sonnenberger, N.; Enke, D.; Beiner, M.; Steinhart, M. Morphology of Porous Hosts Directs Preferred Polymorph Formation and Influences Kinetics of Solid/Solid Transitions of Confined Pharmaceuticals. *Cryst. Growth Des.* **2014**, *14*, 78−86.
(76) Kong, X.; Shayan, K.; Hua, S.; Strauf, S.; Lee, S. S. Complete Suppression of Detrimental Polymorph Transitions in All-Inorganic Perovskites via Nanoconfinement. *ACS Appl. Energy Mater.* **2019**, *2*, 2948−2955.
(77) Rengarajan, G. T.; Enke, D.; Steinhart, M.; Beiner, M. Size-Dependent Growth of Polymorphs in Nanopores and Ostwald's Step Rule of Stages. *Phys. Chem. Chem. Phys.* **2011**, *13*, 21367−21374.
(78) McHale, J. M.; Auroux, A.; Perrotta, A. J.; Navrotsky, A. Surface Energies and Thermodynamic Phase Stability in Nanocrystalline Aluminas. *Science* **1997**, *277*, 788−789.
(79) Garvie, R. C. Stabilization of the Tetragonal Structure in Zirconia Microcrystals. *J. Phys. Chem.* **1978**, *82*, 218−224.
(80) Kong, X.; Shayan, K.; Lee, S.; Ribeiro, C.; Strauf, S.; Lee, S. S. Remarkable Long-Term Stability of Nanoconfined Metal-Halide Perovskite Crystals against Degradation and Polymorph Transitions. *Nanoscale* **2018**, *10*, 8320−8328.
(81) Fu, D.; Suzuki, H.; Ishikawa, K. Size-Induced Phase Transition in Nanocrystals: Raman Scattering Study. *Phys. Rev. B - Condens. Matter Mater. Phys.* **2000**, *62*, 3125−3129.
(82) Ayyub, P.; Palkar, SV. R.; Chattopadhyay, S.; Multani, M. Effect of Crystal Size Reduction on Lattice Symmetry and Cooperative Properties. *Phys. Rev. B* **1995**, *51*, 6135−6138.
(83) Gibbs, J. W. *The Scientific Papers of J. Willard Gibbs*; Dover Publications: New York, 1961.
(84) Wulff, G. XXV. Zur Frage Der Geschwindigkeit Des Wachsthums und der Auflösung der Krystallflächen. *Z. Krist. - Cryst. Mater.* **1901**, *34*, 449−530.
(85) Dandekar, P.; Kuvadia, Z. B.; Doherty, M. F. Engineering Crystal Morphology. *Annu. Rev. Mater. Res.* **2013**, *43*, 359−386.

DOI: 10.1021/acs.chemmater.9b01707
Chem. Mater. 2019, 31, 4953−4970

(86) Shtukenberg, A. G.; Lee, S. S.; Kahr, B.; Ward, M. D. Manipulating Crystallization with Molecular Additives. *Annu. Rev. Chem. Biomol. Eng.* **2014**, *5*, 77−96.
(87) Hamilton, B. D.; Weissbuch, I.; Lahav, M.; Hillmyer, M. A.; Ward, M. D. Manipulating Crystal Orientation in Nanoscale Cylindrical Pores by Stereochemical Inhibition. *J. Am. Chem. Soc.* **2009**, *131*, 2588−2596.
(88) Jayasekara, I.; Poyner, M.; Teeters, D. Investigation of a Nanoconfined, Ceramic Composite. *Electrochim. Acta* **2017**, *247*, 1147−1154.
(89) Steinhart, M.; Göring, P.; Dernaika, H.; Prabhukaran, M.; Gösele, U.; Hempel, E.; Thurn-Albrecht, T. Coherent Kinetic Control over Crystal Orientation in Macroscopic Ensembles of Polymer Nanorods and Nanotubes. *Phys. Rev. Lett.* **2006**, *97*, No. 027801.
(90) Steinhart, M.; Senz, S.; Wehrspohn, R. B.; Gösele, U.; Wendorff, J. H. Curvature-Directed Crystallization of Poly(Vinylidene Difluoride) in Nanotube Walls. *Macromolecules* **2003**, *36*, 3646−3651.
(91) Ryu, S. H.; Ahn, H.; Shin, T. J.; Yoon, D. K. Direct Observation of Liquid Crystal Phases under Nanoconfinement: A Grazing Incidence X-Ray Diffraction Study. *Liq. Cryst.* **2017**, *44*, 713−721.
(92) Lee, M. M.; Teuscher, J.; Miyasaka, T.; Murakami, T. N.; Snaith, H. J. Efficient Hybrid Solar Cells Based on Meso-Superstructured Organometal Halide Perovskites. *Science* **2012**, *338*, 643−647.
(93) National Renewable Energy Laboratory *Best Research-Cell Efficiencies*; https://www.nrel.gov/pv/cell-efficiency.html (accessed March 20, 2019).
(94) Park, B.-W.; Seok, S. Il; Lee, D. U.; Shin, S. S.; Seo, J.; Jung, E. H.; Kim, Y. C.; Jeon, N. J.; Yang, W. S.; Kim, E. K.; Noh, J. H. Iodide Management in Formamidinium-Lead-Halide−Based Perovskite Layers for Efficient Solar Cells. *Science* **2017**, *356*, 1376−1379.
(95) Whitaker, J. B.; Wheeler, L. M.; Ryter, J.; Dou, B.; Garner, S. M.; Moore, D. T.; Breslin, N. J.; Tassone, C. J.; Zhu, K.; Barnes, F. S.; van Hest, M. F. A. M.; Shaheen, S. E.; Berry, J. J.; Bruening, K. Roll-to-Roll Printing of Perovskite Solar Cells. *ACS Energy Lett.* **2018**, *3*, 2558−2565.
(96) Myoung, N.; Cho, H.; Kim, T.-S.; Im, S. H.; Lee, C.-L.; Heo, J. H.; Kim, Y.-H.; Lee, T.-W. Multicolored Organic/Inorganic Hybrid Perovskite Light-Emitting Diodes. *Adv. Mater.* **2015**, *27*, 1248−1254.
(97) Zhu, H.; Fu, Y.; Meng, F.; Wu, X.; Gong, Z.; Ding, Q.; Gustafsson, M. V.; Trinh, M. T.; Jin, S.; Zhu, X. Y. Lead Halide Perovskite Nanowire Lasers with Low Lasing Thresholds and High Quality Factors. *Nat. Mater.* **2015**, *14*, 636−642.
(98) Dou, L.; Yang, Y. M.; You, J.; Hong, Z.; Chang, W. H.; Li, G.; Yang, Y. Solution-Processed Hybrid Perovskite Photodetectors with High Detectivity. *Nat. Commun.* **2014**, *5*, 5404.
(99) Li, D.; Wang, G.; Cheng, H.-C.; Chen, C.-Y.; Wu, H.; Liu, Y.; Huang, Y.; Duan, X. Size-Dependent Phase Transition in Methylammonium Lead Iodide Perovskite Microplate Crystals. *Nat. Commun.* **2016**, *7*, 11330.
(100) Stoumpos, C. C.; Malliakas, C. D.; Kanatzidis, M. G. Semiconducting Tin and Lead Iodide Perovskites with Organic Cations: Phase Transitions, High Mobilities, and near-Infrared Photoluminescent Properties. *Inorg. Chem.* **2013**, *52*, 9019−9038.
(101) Wehrenfennig, C.; Liu, M.; Snaith, H. J.; Johnston, M. B.; Herz, L. M. Charge Carrier Recombination Channels in the Low-Temperature Phase of Organic-Inorganic Lead Halide Perovskite Thin Films. *APL Mater.* **2014**, *2*, No. 081513.
(102) D'Innocenzo, V.; Grancini, G.; Alcocer, M. J. P.; Kandada, A. R. S.; Stranks, S. D.; Lee, M. M.; Lanzani, G.; Snaith, H. J.; Petrozza, A. Excitons versus Free Charges in Organo-Lead Tri-Halide Perovskites. *Nat. Commun.* **2014**, *5*, 3586.
(103) Galkowski, K.; Mitioglu, A.; Miyata, A.; Plochocka, P.; Portugall, O.; Eperon, G. E.; Wang, J. T.-W.; Stergiopoulos, T.; Stranks, S. D.; Snaith, H. J.; Nicholas, R. J. Determination of the Exciton Binding Energy and Effective Masses for Methylammonium and Formamidinium Lead Tri-Halide Perovskite Semiconductors. *Energy Environ. Sci.* **2016**, *9*, 962−970.
(104) Borriello, I.; Cantele, G.; Ninno, D. *Ab Initio* Investigation of Hybrid Organic-Inorganic Perovskites Based on Tin Halides. *Phys. Rev. B: Condens. Matter Mater. Phys.* **2008**, *77*, 235214.
(105) Tonui, P.; Oseni, S. O.; Sharma, G.; Yan, Q.; Tessema Mola, G. Perovskites Photovoltaic Solar Cells: An Overview of Current Status. *Renewable Sustainable Energy Rev.* **2018**, *91*, 1025−1044.
(106) Gu, L.; Tavakoli, M. M.; Zhang, D.; Zhang, Q.; Waleed, A.; Xiao, Y.; Tsui, K. H.; Lin, Y.; Liao, L.; Wang, J.; Fan, Z. 3D Arrays of 1024-Pixel Image Sensors Based on Lead Halide Perovskite Nanowires. *Adv. Mater.* **2016**, *28*, 9713−9721.
(107) Meng, K.; Gao, S.; Wu, L.; Wang, G.; Liu, X.; Chen, G.; Liu, Z.; Chen, G. Two-Dimensional Organic-Inorganic Hybrid Perovskite Photonic Films. *Nano Lett.* **2016**, *16*, 4166−4173.
(108) Kulbak, M.; Cahen, D.; Hodes, G. How Important Is the Organic Part of Lead Halide Perovskite Photovoltaic Cells? Efficient $CsPbBr_3$ Cells. *J. Phys. Chem. Lett.* **2015**, *6*, 2452−2456.
(109) Liang, J.; Wang, C.; Wang, Y.; Xu, Z.; Lu, Z.; Ma, Y.; Zhu, H.; Hu, Y.; Xiao, C.; Yi, X.; Zhu, G.; Lv, H.; Ma, L.; Chen, T.; Tie, Z.; Jin, Z.; Liu, J. All-Inorganic Perovskite Solar Cells. *J. Am. Chem. Soc.* **2016**, *138*, 15829−15832.
(110) Marronnier, A.; Roma, G.; Boyer-Richard, S.; Pedesseau, L.; Jancu, J. M.; Bonnassieux, Y.; Katan, C.; Stoumpos, C. C.; Kanatzidis, M. G.; Even, J. Anharmonicity and Disorder in the Black Phases of Cesium Lead Iodide Used for Stable Inorganic Perovskite Solar Cells. *ACS Nano* **2018**, *12*, 3477−3486.
(111) Da Silva, E. L.; Skelton, J. M.; Parker, S. C.; Walsh, A. Phase Stability and Transformations in the Halide Perovskite $CsSnI_3$. *Phys. Rev. B: Condens. Matter Mater. Phys.* **2015**, *91*, 144107.
(112) Møller, C. K. Crystal Structure and Photoconductivity of Cæsium Plumbohalides. *Nature* **1958**, *182*, 1436.
(113) Swarnkar, A.; Marshall, A. R.; Sanehira, E. M.; Chernomordik, B. D.; Moore, D. T.; Christians, J. A.; Chakrabarti, T.; Luther, J. M. Quantum Dot-Induced Phase Stabilization of α-$CsPbI_3$ perovskite for High-Efficiency Photovoltaics. *Science* **2016**, *354*, 92−95.
(114) Liu, F.; Zhang, Y.; Ding, C.; Kobayashi, S.; Izuishi, T.; Nakazawa, N.; Toyoda, T.; Ohta, T.; Hayase, S.; Minemoto, T.; Yoshino, K.; Dai, S.; Shen, Q. Highly Luminescent Phase-Stable $CsPbI_3$ Perovskite Quantum Dots Achieving Near 100% Absolute Photoluminescence Quantum Yield. *ACS Nano* **2017**, *11*, 10373−10383.
(115) Li, X.; Wu, Y.; Zhang, S.; Cai, B.; Gu, Y.; Song, J.; Zeng, H. $CsPbX_3$ Quantum Dots for Lighting and Displays: Room-Temperature Synthesis, Photoluminescence Superiorities, Underlying Origins and White Light-Emitting Diodes. *Adv. Funct. Mater.* **2016**, *26*, 2435−2445.
(116) Liu, F.; Ding, C.; Zhang, Y.; Ripolles, T. S.; Kamisaka, T.; Toyoda, T.; Hayase, S.; Minemoto, T.; Yoshino, K.; Dai, S.; Yanagida, M.; Noguchi, H.; Shen, Q. Colloidal Synthesis of Air-Stable Alloyed $CsSn_{1-x}Pb_xI_3$ Perovskite Nanocrystals for Use in Solar Cells. *J. Am. Chem. Soc.* **2017**, *139*, 16708−16719.
(117) Sutton, R. J.; Filip, M. R.; Haghighirad, A. A.; Sakai, N.; Wenger, B.; Giustino, F.; Snaith, H. J. Cubic or Orthorhombic? Revealing the Crystal Structure of Metastable Black-Phase $CsPbI_3$ by Theory and Experiment. *ACS Energy Lett.* **2018**, *3*, 1787−1794.
(118) Shpatz Dayan, A.; Cohen, B. El; Aharon, S.; Tenailleau, C.; Wierzbowska, M.; Etgar, L. Enhancing Stability and Photostability of $CsPbI_3$ by Reducing Its Dimensionality. *Chem. Mater.* **2018**, *30*, 8017−8024.
(119) Zhao, B.; Jin, S. F.; Huang, S.; Liu, N.; Ma, J. Y.; Xue, D. J.; Han, Q.; Ding, J.; Ge, Q. Q.; Feng, Y.; Hu, J. S. Thermodynamically Stable Orthorhombic γ-$CsPbI_3$ Thin Films for High-Performance Photovoltaics. *J. Am. Chem. Soc.* **2018**, *140*, 11716−11725.
(120) Waleed, A.; Tavakoli, M. M.; Gu, L.; Hussain, S.; Zhang, D.; Poddar, S.; Wang, Z.; Zhang, R.; Fan, Z. All Inorganic Cesium Lead Iodide Perovskite Nanowires with Stabilized Cubic Phase at Room Temperature and Nanowire Array-Based Photodetectors. *Nano Lett.* **2017**, *17*, 4951−4957.
(121) Ma, S.; Kim, S. H.; Jeong, B.; Kwon, H.; Yun, S.; Jang, G.; Yang, H.; Park, C.; Lee, D.; Moon, J. Strain-Mediated Phase

DOI: 10.1021/acs.chemmater.9b01707
Chem. Mater. 2019, 31, 4953−4970

Stabilization: A New Strategy for Ultrastable a-$CsPbI_3$ Perovskite by Nanoconfined Growth. *Small* **2019**, *15*, 1900219.
(122) Kwon, H. C.; Kim, A.; Lee, H.; Lee, D.; Jeong, S.; Moon, J. Parallelized Nanopillar Perovskites for Semitransparent Solar Cells Using an Anodized Aluminum Oxide Scaffold. *Adv. Energy Mater.* **2016**, *6*, 1601055.
(123) Waleed, A.; Tavakoli, M. M.; Gu, L.; Wang, Z.; Zhang, D.; Manikandan, A.; Zhang, Q.; Zhang, R.; Chueh, Y. L.; Fan, Z. Lead-Free Perovskite Nanowire Array Photodetectors with Drastically Improved Stability in Nanoengineering Templates. *Nano Lett.* **2017**, *17*, 523−530.
(124) Horváth, E.; Spina, M.; Szekrényes, Z.; Kamarás, K.; Gaal, R.; Gachet, D.; Forró, L. Nanowires of Methylammonium Lead Iodide ($CH_3NH_3PbI_3$) Prepared by Low Temperature Solution-Mediated Crystallization. *Nano Lett.* **2014**, *14*, 6761−6766.
(125) Gu, L.; Tavakoli, M. M.; Zhang, D.; Zhang, Q.; Waleed, A.; Xiao, Y.; Tsui, K. H.; Lin, Y.; Liao, L.; Wang, J.; Fan, Z. 3D Arrays of 1024-Pixel Image Sensors based on Lead Halide Perovskite Nanowires. *Adv. Mater.* **2016**, *28*, 9713−9721.
(126) Sundar, V. C.; Zaumseil, J.; Podzorov, V.; Menard, E.; Willett, R. L.; Someya, T.; Gershenson, M. E.; Rogers, J. A. Elastomeric Transistor Stamps: Reversible Probing of Charge Transport in Organic Crystals. *Science* **2004**, *303*, 1644−1646.
(127) Anthony, J. E.; Brooks, J. S.; Eaton, D. L.; Parkin, S. R. Functionalized Pentacene: Improved Electronic Properties from Control of Solid-State Order. *J. Am. Chem. Soc.* **2001**, *123*, 9482−9483.
(128) Bai, X.; Zong, K.; Ly, J.; Mehta, J. S.; Hand, M.; Molnar, K.; Lee, S.; Kahr, B.; Mativetsky, J. M.; Briseno, A.; Lee, S. S. Orientation Control of Solution-Processed Organic Semiconductor Crystals to Improve Out-of-Plane Charge Mobility. *Chem. Mater.* **2017**, *29*, 7571−7578.
(129) Jimison, L. H.; Toney, M. F.; McCulloch, I.; Heeney, M.; Salleo, A. Charge-Transport Anisotropy Due to Grain Boundaries in Directionally Crystallized Thin Films of Regioregular Poly(3-Hexylthiophene). *Adv. Mater.* **2009**, *21*, 1568−1572.
(130) Sirringhaus, H.; Brown, P. J.; Friend, R. H.; Nielsen, M. M.; Bechgaard, K.; Langeveld-Voss, B. M. W.; Spiering, A. J. H.; Janssen, R. A. J.; Meijer, E. W.; Herwig, P.; de Leeuw, D. M. Two-Dimensional Charge Transport in Self-Organized, High-Mobility Conjugated Polymers. *Nature* **1999**, *401*, 685−688.
(131) Abidian, M. R.; Kim, D.-H.; Martin, D. C. Conducting-Polymer Nanotubes for Controlled Drug Release. *Adv. Mater.* **2006**, *18*, 405−409.
(132) Malik, S.; Nandi, A. K. Crystallization Mechanism of Regioregular Poly(3-Alkyl Thiophene)S. *J. Polym. Sci., Part B: Polym. Phys.* **2002**, *40*, 2073−2085.
(133) Biniek, L.; Leclerc, N.; Heiser, T.; Bechara, R.; Brinkmann, M. Large Scale Alignment and Charge Transport Anisotropy of PBTTT Films Oriented by High Temperature Rubbing. *Macromolecules* **2013**, *46*, 4014−4023.
(134) Lee, M. J.; Gupta, D.; Zhao, N.; Heeney, M.; McCulloch, I.; Sirringhaus, H. Anisotropy of Charge Transport in a Uniaxially Aligned and Chain-Extended, High-Mobility, Conjugated Polymer Semiconductor. *Adv. Funct. Mater.* **2011**, *21*, 932−940.
(135) Zhang, N. X.; Ren, A. M.; Ji, L. F.; Zhang, S. F.; Guo, J. F. Theoretical Investigations on Molecular Packing Motifs and Charge Transport Properties of a Family of Trialkylsilylethynyl-Modified Pentacenes/Anthradithiophenes. *J. Phys. Chem. C* **2018**, *122*, 18880−18894.
(136) Thorley, K. J.; Finn, T. W.; Jarolimek, K.; Anthony, J. E.; Risko, C. Theory-Driven Insight into the Crystal Packing of Trialkylsilylethynyl Pentacenes. *Chem. Mater.* **2017**, *29*, 2502−2512.
(137) García-Frutos, E. M.; Gutierrez-Puebla, E.; Monge, M. A.; Ramírez, R.; Andrés, P. d.; Andrés, A. d.; Ramírez, R.; Gómez-Lor, B. Crystal Structure and Charge-Transport Properties of N-Trimethyl-triindole: Novel p-Type Organic Semiconductor Single Crystals. *Org. Electron.* **2009**, *10*, 643−652.
(138) Miyahara, T.; Shimizu, M. Single Crystal Growth of Organic Semiconductors by the Repeated Solid Solvent Growth Method Using Melted Anthracene as a Solvent. *J. Cryst. Growth* **2001**, *229*, 553−557.
(139) Shaw, L.; Hayoz, P.; Diao, Y.; Reinspach, J. A.; To, J. W. F.; Toney, M. F.; Weitz, R. T.; Bao, Z. Direct Uniaxial Alignment of a Donor-Acceptor Semiconducting Polymer Using Single-Step Solution Shearing. *ACS Appl. Mater. Interfaces* **2016**, *8*, 9285−9296.
(140) Diao, Y.; Shaw, L.; Bao, Z.; Mannsfeld, S. C. B. Morphology Control Strategies for Solution-Processed Organic Semiconductor Thin Films. *Energy Environ. Sci.* **2014**, *7*, 2145−2159.
(141) Giri, G.; Delongchamp, D. M.; Reinspach, J.; Fischer, D. A.; Richter, L. J.; Xu, J.; Benight, S.; Ayzner, A.; He, M.; Fang, L.; Xue, G.; Toney, M. F.; Bao, Z. Effect of Solution Shearing Method on Packing and Disorder of Organic Semiconductor Polymers. *Chem. Mater.* **2015**, *27*, 2350−2359.
(142) Lee, S. S.; Tang, S. B.; Smilgies, D. M.; Woll, A. R.; Loth, M. A.; Mativetsky, J. M.; Anthony, J. E.; Loo, Y. L. Guiding Crystallization around Bends and Sharp Corners. *Adv. Mater.* **2012**, *24*, 2692−2698.
(143) Lee, S. S.; Mativetsky, J. M.; Loth, M. A.; Anthony, J. E.; Loo, Y. Quantifying Resistances across Interspherulite Boundaries in Solution-Processed Organic Semiconductor Thin Films. *ACS Nano* **2012**, *6*, 9879−9886.
(144) Miyajima, D.; Araoka, F.; Takezoe, H.; Kim, J.; Kato, K.; Takata, M.; Aida, T. Electric-Field-Responsive Handle for Large-Area Orientation of Discotic Liquid-Crystalline Molecules in Millimeter-Thick Films. *Angew. Chem., Int. Ed.* **2011**, *50*, 7865−7869.
(145) Murphy, A. R.; Fréchet, J. M. J. Organic Semiconducting Oligomers for Use in Thin Film Transistors. *Chem. Rev.* **2007**, *107*, 1066−1096.
(146) Menard, E.; Meitl, M. A.; Sun, Y.; Park, J.-U.; Shir, D. J.-L.; Nam, Y.-S.; Jeon, S.; Rogers, J. A. Micro- and Nanopatterning Techniques for Organic Electronic and Optoelectronic Systems. *Chem. Rev.* **2007**, *107*, 1117−1160.
(147) Giri, G.; Park, S.; Vosgueritchian, M.; Shulaker, M. M.; Bao, Z. High-Mobility, Aligned Crystalline Domains of TIPS-Pentacene with Metastable Polymorphs Through Lateral Confinement of Crystal Growth. *Adv. Mater.* **2014**, *26*, 487−493.
(148) Bruinink, C. M.; Péter, M.; Maury, P. A.; de Boer, M.; Kuipers, L.; Huskens, J.; Reinhoudt, D. N. Capillary Force Lithography: Fabrication of Functional Polymer Templates as Versatile Tools for Nanolithography. *Adv. Funct. Mater.* **2006**, *16*, 1555−1565.
(149) Jo, P. S.; Vailionis, A.; Park, Y. M.; Salleo, A. Scalable Fabrication of Strongly Textured Organic Semiconductor Micro-patterns by Capillary Force Lithography. *Adv. Mater.* **2012**, *24*, 3269−3274.
(150) Park, K. S.; Cho, B.; Baek, J.; Hwang, J. K.; Lee, H.; Sung, M. M. Single-Crystal Organic Nanowire Electronics by Direct Printing from Molecular Solutions. *Adv. Funct. Mater.* **2013**, *23*, 4776−4784.
(151) Watanabe, S.; Fujita, T.; Ribierre, J.-C.; Takaishi, K.; Muto, T.; Adachi, C.; Uchiyama, M.; Aoyama, T.; Matsumoto, M. Microcrystallization of a Solution-Processable Organic Semiconductor in Capillaries for High-Performance Ambipolar Field-Effect Transistors. *ACS Appl. Mater. Interfaces* **2016**, *8*, 17574−17582.
(152) Kim, K.; Hong, J.; Hahm, S. G.; Rho, Y.; An, T. K.; Kim, S. H.; Park, C. E. Facile and Microcontrolled Blade Coating of Organic Semiconductor Blends for Uniaxial Crystal Alignment and Reliable Flexible Organic Field-Effect Transistors. *ACS Appl. Mater. Interfaces* **2019**, *11*, 13481−13490.
(153) Kim, K.; Rho, Y.; Kim, Y.; Kim, S. H.; Hahm, S. G.; Park, C. E. A Lattice-Strained Organic Single-Crystal Nanowire Array Fabricated via Solution-Phase Nanograting-Assisted Pattern Transfer for Use in High-Mobility Organic Field-Effect Transistors. *Adv. Mater.* **2016**, *28*, 3209−3215.
(154) Park, K. S.; Salunkhe, S. M.; Lim, I.; Cho, C.-G.; Han, S.-H.; Sung, M. M. High-Performance Air-Stable Single-Crystal Organic

DOI: 10.1021/acs.chemmater.9b01707
Chem. Mater. 2019, 31, 4953−4970

Nanowires Based on a New Indolocarbazole Derivative for Field-Effect Transistors. *Adv. Mater.* **2013**, *25*, 3351−3356.
(155) Kim, K.; Jang, M.; Lee, M.; An, T. K.; Anthony, J. E.; Kim, S. H.; Yang, H.; Park, C. E. Unified Film Patterning and Annealing of an Organic Semiconductor with Micro-Grooved Wet Stamps. *J. Mater. Chem. C* **2016**, *4*, 6996−7003.
(156) Nguyen, K. V.; Lee, J. H.; Lee, S. C.; Ku, G. M.; Lee, W. H. Simultaneous Control of Molecular Orientation and Patterning of Small-Molecule Organic Semiconductors for Organic Transistors. *Org. Electron.* **2017**, *41*, 107−113.
(157) Kim, A.; Jang, K.-S.; Kim, J.; Won, J. C.; Yi, M. H.; Kim, H.; Yoon, D. K.; Shin, T. J.; Lee, M.-H.; Ka, J.-W.; Kim, Y. H. Solvent-Free Directed Patterning of a Highly Ordered Liquid Crystalline Organic Semiconductor via Template-Assisted Self-Assembly for Organic Transistors. *Adv. Mater.* **2013**, *25*, 6219−6225.
(158) Aryal, M.; Trivedi, K.; Hu, W. W. Nano-Confinement Induced Chain Alignment in Ordered P3HT Nanostructures Defined by Nanoimprint Lithography. *ACS Nano* **2009**, *3*, 3085−3090.
(159) Kushi, S.; Tsukada, R.; Noguchi, K.; Shimomura, T. Crystallization of Poly(3-Hexylthiophene) Nanofiber in a Narrow Groove. *Polymers (Basel, Switz.)* **2016**, *8*, 231.
(160) Beh, W. S.; Kim, I. T.; Qin, D.; Xia, Y.; Whitesides, G. M. Formation of Patterned Microstructures of Conducting Polymers by Soft Lithography, and Applications in Microelectronic Device Fabrication. *Adv. Mater.* **1999**, *11*, 1038−1041.
(161) Johnston, D. E.; Yager, K. G.; Hlaing, H.; Lu, X.; Ocko, B. M.; Black, C. T. Nanostructured Surfaces Frustrate Polymer Semiconductor Molecular Orientation. *ACS Nano* **2014**, *8*, 243−249.
(162) Oh, S.; Hayakawa, R.; Chikyow, T.; Wakayama, Y. Nanochannel Effect in Polymer Nanowire Transistor with Highly Aligned Polymer Chains. *Appl. Phys. Lett.* **2015**, *106*, 243301.
(163) Wei, S.; Zhang, Y.; Liu, J.; Li, X.; Wu, Y.; Wei, H.; Weng, Y.; Gao, X.; Li, Y.; Wang, S.-D.; Hu, Z. Large Modulation of Charge Transport Anisotropy by Controlling the Alignment of π-π Stacks in Diketopyrrolopyrrole-Based Polymers. *Adv. Mater. Interfaces* **2015**, *2*, 1500153.
(164) Gonzalez Arellano, D. L.; Kolewe, K. W.; Champagne, V. K., III; Kurtz, I. S.; Burnett, E. K.; Zakashansky, J. A.; Arisoy, F. D.; Briseno, A. L.; Schiffman, J. D. Gecko-Inspired Biocidal Organic Nanocrystals Initiated from a Pencil-Drawn Graphite Template. *Sci. Rep.* **2018**, *8*, 11618.
(165) Kim, K.; Santos, E. J. G.; Lee, T. H.; Nishi, Y.; Bao, Z. Epitaxially Grown Strained Pentacene Thin Film on Graphene Membrane. *Small* **2015**, *11*, 2037−2043.
(166) Jo, S. B.; Kim, H. H.; Lee, H.; Kang, B.; Lee, S.; Sim, M.; Kim, M.; Lee, W. H.; Cho, K. Boosting Photon Harvesting in Organic Solar Cells with Highly Oriented Molecular Crystals via Graphene-Organic Heterointerface. *ACS Nano* **2015**, *9*, 8206−8219.
(167) Zhang, Y.; Diao, Y.; Lee, H.; Mirabito, T. J.; Johnson, R. W.; Puodziukynaite, E.; John, J.; Carter, K. R.; Emrick, T.; Mannsfeld, S. C. B.; Briseno, A. L. Intrinsic and Extrinsic Parameters for Controlling the Growth of Organic Single-Crystalline Nanopillars in Photovoltaics. *Nano Lett.* **2014**, *14*, 5547−5554.
(168) Mativetsky, J. M.; Wang, H.; Lee, S. S.; Whittaker-Brooks, L.; Loo, Y.-L. Face-on Stacking and Enhanced out-of-Plane Hole Mobility in Graphene-Templated Copper Phthalocyanine. *Chem. Commun.* **2014**, *50*, 5319−5321.
(169) Wang, Y.; Torres, J. A.; Stieg, A. Z.; Jiang, S.; Yeung, M. T.; Rubin, Y.; Chaudhuri, S.; Duan, X.; Kaner, R. B. Graphene-Assisted Solution Growth of Vertically Oriented Organic Semiconducting Single Crystals. *ACS Nano* **2015**, *9*, 9486−9496.
(170) Wu, H.; Yang, J.; Cao, S.; Huang, L.; Chen, L. Ordered Organic Nanostructures Fabricated from Anodic Alumina Oxide Templates for Organic Bulk-Heterojunction Photovoltaics. *Macromol. Chem. Phys.* **2014**, *215*, 584−596.
(171) Haberkorn, N.; Lechmann, M. C.; Sohn, B. H.; Char, K.; Gutmann, J. S.; Theato, P. Templated Organic and Hybrid Materials for Optoelectronic Applications. *Macromol. Rapid Commun.* **2009**, *30*, 1146−1166.
(172) Martin, C. R. Template Synthesis of Electronically Conductive Polymer Nanostructures. *Acc. Chem. Res.* **1995**, *28*, 61−68.
(173) Fu, M.; Zhu, Y.; Tan, R.; Shi, G. Aligned Polythiophene Micro- and Nanotubules. *Adv. Mater.* **2001**, *13*, 1874−1877.
(174) Cao, J.; Sun, J.; Shi, G.; Chen, H.; Zhang, Q.; Wang, D.; Wang, M. Photovoltaic Properties of Polythiophene Nano-Tubule Films. *Mater. Chem. Phys.* **2003**, *82*, 44−48.
(175) Joo, J.; Kim, B. H.; Park, D. H.; Kim, H. S.; Seo, D. S.; Shim, J. H.; Lee, S. J.; Ryu, K. S.; Kim, K.; Jin, J.-I.; Lee, T. J.; Lee, C. J. Fabrication and Applications of Conducting Polymer Nanotube, Nanowire, Nanohole, and Double Wall Nanotube. *Synth. Met.* **2005**, *153*, 313−316.
(176) Park, D. H.; Kim, B. H.; Jang, M. G.; Bae, K. Y.; Joo, J. Characteristics and Photoluminescence of Nanotubes and Nanowires of Poly (3-methylthiophene). *Appl. Phys. Lett.* **2005**, *86*, 113116.
(177) Park, D. H.; Kim, B. H.; Jang, M. K.; Bae, K. Y.; Lee, S. J.; Joo, J. Synthesis and Characterization of Polythiophene and Poly (3-Methylthiophene) Nanotubes and Nanowires. *Synth. Met.* **2005**, *153*, 341−344.
(178) Berdichevsky, Y.; Lo, Y.-H. Polypyrrole Nanowire Actuators. *Adv. Mater.* **2006**, *18*, 122−125.
(179) Cho, S. I.; Kwon, W. J.; Choi, S.-J.; Kim, P.; Park, S.-A.; Kim, J.; Son, S. J.; Xiao, R.; Kim, S.-H.; Lee, S. B. Nanotube-Based Ultrafast Electrochromic Display. *Adv. Mater.* **2005**, *17*, 171−175.
(180) Han, M. G.; Foulger, S. H. 1-Dimensional Structures of Poly(3,4-Ethylenedioxythiophene) (PEDOT): A Chemical Route to Tubes, Rods, Thimbles, and Belts. *Chem. Commun.* **2005**, 3092−3094.
(181) Xiao, R.; Cho, S. Il; Liu, R.; Lee, S. B. Controlled Electrochemical Synthesis of Conductive Polymer Nanotube Structures. *J. Am. Chem. Soc.* **2007**, *129*, 4483−4489.
(182) Lin, H.-A.; Luo, S.-C.; Zhu, B.; Chen, C.; Yamashita, Y.; Yu, H. Molecular or Nanoscale Structures? The Deciding Factor of Surface Properties on Functionalized Poly(3,4-Ethylenedioxythiophene) Nanorod Arrays. *Adv. Funct. Mater.* **2013**, *23*, 3212−3219.
(183) Zhang, L.; Meng, F.; Chen, Y.; Liu, J.; Sun, Y.; Luo, T.; Li, M.; Liu, J. A Novel Ammonia Sensor Based on High Density, Small Diameter Polypyrrole Nanowire Arrays. *Sens. Actuators, B* **2009**, *142*, 204−209.
(184) Huesmann, D.; DiCarmine, P. M.; Seferos, D. S. Template-Synthesized Nanostructure Morphology Influenced by Building Block Structure. *J. Mater. Chem.* **2011**, *21*, 408−413.
(185) Dauginet-De Pra, L.; Ferain, E.; Legras, R.; Demoustier-Champagne, S. Fabrication of a New Generation of Track-Etched Templates and Their Use for the Synthesis of Metallic and Organic Nanostructures. *Nucl. Instrum. Methods Phys. Res., Sect. B* **2002**, *196*, 81−88.
(186) Dauginet, L.; Duwez, A.-S.; Legras, R.; Demoustier-Champagne, S. Surface Modification of Polycarbonate and Poly-(Ethylene Terephthalate) Films and Membranes by Polyelectrolyte Deposition. *Langmuir* **2001**, *17*, 3952−3957.
(187) Li, X.; Tian, S.; Ping, Y.; Kim, D. H.; Knoll, W. One-Step Route to the Fabrication of Highly Porous Polyaniline Nanofiber Films by Using PS-b-PVP Diblock Copolymers as Templates. *Langmuir* **2005**, *21*, 9393−9397.
(188) Wang, Z.-L.; Guo, R.; Ding, L.-X.; Tong, Y.-X.; Li, G.-R. Controllable Template-Assisted Electrodeposition of Single- and Multi-Walled Nanotube Arrays for Electrochemical Energy Storage. *Sci. Rep.* **2013**, *3*, 1204.
(189) Kang, H.; Lee, H.; Kwak, J. Electrodeposition of Polypyrrole Nanowires within Vertically Oriented Mesoporous Silica Template. *J. Korean Electrochem. Soc.* **2011**, *14*, 22−26.
(190) Feng, Z. Q.; Wu, J.; Cho, W.; Leach, M. K.; Franz, E. W.; Naim, Y. I.; Gu, Z. Z.; Corey, J. M.; Martin, D. C. Highly Aligned Poly(3,4-Ethylene Dioxythiophene) (PEDOT) Nano- and Microscale Fibers and Tubes. *Polymer* **2013**, *54*, 702−708.
(191) Estrany, F.; Calvet, A.; Del Valle, L. J.; Puiggalí, J.; Alemán, C. A Multi-Step Template-Assisted Approach for the Formation of Conducting Polymer Nanotubes onto Conducting Polymer Films. *Polym. Chem.* **2016**, *7*, 3540−3550.

DOI: 10.1021/acs.chemmater.9b01707
Chem. Mater. 2019, 31, 4953−4970

(192) Coakley, K. M.; Srinivasan, B. S.; Ziebarth, J. M.; Goh, C.; Liu, Y.; McGehee, M. D. Enhanced Hole Mobility in Regioregular Polythiophene Infiltrated in Straight Nanopores. *Adv. Funct. Mater.* **2005**, *15*, 1927−1932.
(193) Kim, J. S.; Park, Y.; Lee, D. Y.; Lee, J. H.; Park, J. H.; Kim, J. K.; Cho, K. Poly(3-Hexylthiophene) Nanorods with Aligned Chain Orientation for Organic Photovoltaics. *Adv. Funct. Mater.* **2010**, *20*, 540−545.
(194) Ding, G.; Wu, Y.; Weng, Y.; Zhang, W.; Hu, Z. Solvent-Assistant Room Temperature Nanoimprinting-Induced Molecular Orientation in Poly(3-Hexylthiophene) Nanopillars. *Macromolecules* **2013**, *46*, 8638−8643.
(195) Byun, J.; Kim, Y.; Jeon, G.; Kim, J. K. Ultrahigh Density Array of Free-Standing Poly(3-Hexylthiophene) Nanotubes on Conducting Substrates via Solution Wetting. *Macromolecules* **2011**, *44*, 8558−8562.
(196) Ding, G.; Li, C.; Li, X.; Wu, Y.; Liu, J.; Li, Y.; Hu, Z.; Li, Y. Quantitative Analysis of the Size Effect of Room Temperature Nanoimprinted P3HT Nanopillar Arrays on the Photovoltaic Performance. *Nanoscale* **2015**, *7*, 11024−11032.
(197) Xiang, W.; Sun, X.; Ren, Z.; Zhang, J.; Li, H.; Yan, S. Diameter and Thermal Treatment Dependent Structure and Optical Properties of Poly(3-Hexylthiophene) Nanotubes. *J. Mater. Chem. C* **2017**, *5*, 8315−8322.
(198) Santos, A.; Formentín, P.; Pallarés, J.; Ferré-Borrull, J.; Marsal, L. F. Fabrication and Characterization of High-Density Arrays of P3HT Nanopillars on ITO/Glass Substrates. *Sol. Energy Mater. Sol. Cells* **2010**, *94*, 1247−1253.
(199) Chen, D.; Zhao, W.; Russell, T. P. P3HT Nanopillars for Organic Photovoltaic Devices Nanoimprinted by AAO Templates. *ACS Nano* **2012**, *6*, 1479−1485.
(200) Wu, H.; Higaki, Y.; Nojima, S.; Takahara, A. Orientation and Crystallization of Regioregular Poly(3-Dodecylthiophene) in Alumina Nanopores. *Soft Matter* **2017**, *13*, 4661−4666.
(201) Steinhart, M.; Zimmermann, S.; Göring, P.; Schaper, A. K.; Gösele, U.; Weder, C.; Wendorff, J. H. Liquid Crystalline Nanowires in Porous Alumina: Geometric Confinement versus Influence of Pore Walls. *Nano Lett.* **2005**, *5*, 429−434.
(202) Duran, H.; Hartmann-Azanza, B.; Steinhart, M.; Gehrig, D.; Laquai, F.; Feng, X.; Müllen, K.; Butt, H. J.; Floudas, G. Arrays of Aligned Supramolecular Wires by Macroscopic Orientation of Columnar Discotic Mesophases. *ACS Nano* **2012**, *6*, 9359−9365.
(203) Pisula, W.; Kastler, M.; Wasserfallen, D.; Davies, R. J.; García-Gutiérrez, M. C.; Müllen, K. From Macro- to Nanoscopic Templating with Nanographenes. *J. Am. Chem. Soc.* **2006**, *128*, 14424−14425.
(204) Martín, J.; Dyson, M.; Reid, O. G.; Li, R.; Nogales, A.; Smilgies, D. M.; Silva, C.; Rumbles, G.; Amassian, A.; Stingelin, N. On the Effect of Confinement on the Structure and Properties of Small-Molecular Organic Semiconductors. *Adv. Electron. Mater.* **2018**, *4*, 1700308.
(205) Abdelsamie, M.; Treat, N. D.; Zhao, K.; McDowell, C.; Burgers, M. A.; Li, R.; Smilgies, D.-M.; Stingelin, N.; Bazan, G. C.; Amassian, A. Toward Additive-Free Small-Molecule Organic Solar Cells: Roles of the Donor Crystallization Pathway and Dynamics. *Adv. Mater.* **2015**, *27*, 7285−7292.
(206) Zong, K.; Ma, Y.; Shayan, K.; Ly, J.; Renjilian, E.; Hu, C.; Strauf, S.; Briseno, A.; Lee, S. S. Directing Solution-Phase Nucleation to Form Organic Semiconductor Vertical Crystal Arrays. *Cryst. Growth Des.* **2019**, *19*, 3461−3468.
(207) Zhang, L.; Fonari, A.; Zhang, Y.; Zhao, G.; Coropceanu, V.; Hu, W.; Parkin, S.; Brédas, J.-L.; Briseno, A. L. Triisopropylsilylethynyl-Functionalized Graphene-Like Fragment Semiconductors: Synthesis, Crystal Packing, and Density Functional Theory Calculations. *Chem. - Eur. J.* **2013**, *19*, 17907−17916.

DOI: 10.1021/acs.chemmater.9b01707
Chem. Mater. 2019, 31, 4953−4970